ACS APPLIED MATERIALS & INTERFACES

www.acsami.org Research Article

Voltage-Switchable Biosensor with Gold Nanoparticles on TiO_2 Nanotubes Decorated with CdS Quantum Dots for the Detection of Cholesterol and H_2O_2

Nilem Khaliq, Muhammad Asim Rasheed, Maaz Khan, Muhammad Maqbool, Mashkoor Ahmad, Shafqat Karim, Amjad Nisar, Patrik Schmuki,* Sung Oh Cho, and Ghafar Ali*

Cite This: *ACS Appl. Mater. Interfaces* 2021, 13, 3653–3668 Read Online

ABSTRACT: A thin layer of gold nanoparticles (Au NPs) sputtered on cadmium sulfide quantum dots (CdS QDs) decorated anodic titanium dioxide nanotubes (TNTs) (Au/CdS QDs/TNTs) was fabricated and explored for the nonenzymatic detection of cholesterol and hydrogen peroxide (H_2O_2). Morphological studies of the sensor revealed the formation of uniform nanotubes decorated with a homogeneously dispersed CdS QDs and Au NPs layer. The electrochemical measurements showed an enhanced electrocatalytic performance with a fast electron transfer (~2 s) between the redox centers of each analyte and electrode surface. The hybrid nanostructure (Au/CdS QDs/TNTs) electrode exhibited about a 6-fold increase in sensitivity for both cholesterol (10,790 μA mM^{-1} cm^{-2}) and H_2O_2 (78,833 μA mM^{-1} cm^{-2}) in analyses compared to the pristine samples. The hybrid electrode utilized different operational potentials for both analytes, which may lead to a voltage-switchable dual-analyte biosensor with a higher selectivity. The biosensor also demonstrated a good reproducibility, thermal stability, and increased shelf life. In addition, the clinical significance of the biosensor was tested for cholesterol and H_2O_2 in real blood samples, which showed maximum relative standard deviations of 1.8 and 2.3%, respectively. These results indicate that a Au/CdS QDs/TNTs-based hybrid nanostructure is a promising choice for an enzyme-free biosensor due to its suitable band gap alignment and higher electrocatalytic activities.

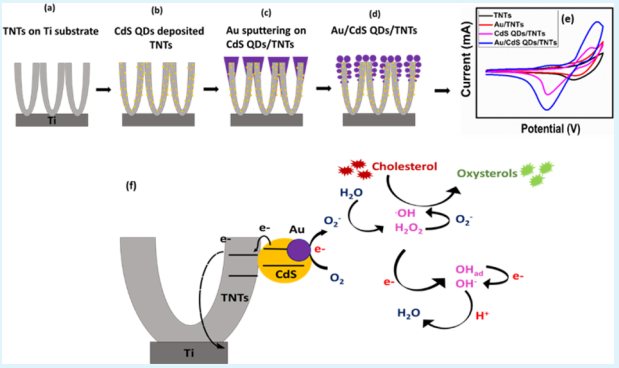

KEYWORDS: *anodization, titanium oxide nanotubes, cadmium sulfide quantum dots, gold nanoparticles, biosensor, amperometry*

INTRODUCTION

In the modern age of health care, the detection of multiple disease biomarkers on a single kit is highly desirable as human health depends on many intricate processes that continuously take place in the body.[1] These processes are dependent on the delicate balance of many physiological, chemical, and biological species. Most of the biological molecules (e.g., H_2O_2) are produced as a result of the enzymatic reaction of other species like glucose, cholesterol, and creatinine. Therefore, the sensitive quantification and analyses of both molecules (e.g., cholesterol and H_2O_2) can be used as an indicator of the progress of the reaction. Cholesterol is an important species, which regulates the processes related to the efficient and healthy function of the heart and relevant organs. Any abnormalities in the human blood cholesterol level can result in several diseases, e.g., coronary heart disease and arteriosclerosis, hypertension, and brain thrombosis.[2,3] On the other hand, H_2O_2, as an important element of biological functions, is usually produced during infection and inflammation in the body and can be used as a potential biomarker for diagnosing these pathological conditions.[4] Moreover, it also plays a vital role in the regulation of cell signaling processes. However, the excessive production of H_2O_2 in the human body leads to some severe diseases including cancer, cardiovascular diseases, Alzheimer, Parkinson, etc.[5] Thus, it is important to investigate the real-time detection of cholesterol and H_2O_2 simultaneously to monitor the human health conditions.

The conventional multiple-analyte electrochemical sensors are mostly based on enzymes where cholesterol oxidase and horseradish peroxidase are popular tag enzymes for cholesterol and H_2O_2 in molecular biology. Although these biosensors offer a higher selectivity, they typically lead to a short device lifetime due to the inherent instability of the enzymes causing

Received: November 9, 2020
Accepted: December 30, 2020
Published: January 13, 2021

https://dx.doi.org/10.1021/acsami.0c19979
ACS Appl. Mater. Interfaces 2021, 13, 3653–3668

denaturation.[6−8] Moreover, in these sensors, a variation in the temperature and pH of the electrolyte during measurements can easily deteriorate their catalytic activities. Therefore, the development of novel materials with higher electrocatalytic properties is highly desirable to reduce the shortcoming of the native enzymes. Nowadays, advancements in nanotechnology lead toward the invention of novel nanostructure materials that have become exceptional substitutes for the enzymes.[9] In the literature, different switchable logic gates-based biosensors have been developed that can be used to detect different biological elements by switching between two states (on/off) in response to an external stimuli, e.g., pH, temperature, voltage, or any combination of them.[10−16] However, these sensors rely on the biorecognition elements, e.g., enzymes, proteins, antibodies, or antigens. These problems can be significantly reduced by using low-dimensional nanomaterials that can be extremely reactive with cholesterol and H_2O_2 in response to any external stimuli, e.g. voltage, to design a sensitive dual-analyte biosensor. For this reason, the selection of the functional materials should be based on which materials can facilitate the selective activation of the sensing gate toward the target analytes. This idea can be evaluated if the biosensing functional materials are active on different externally applied biases for cholesterol and H_2O_2.

The general composition of sensors is based on an electrochemically active material that is attached onto a glassy carbon electrode (GCE) using a conducting polymer binder (e.g., Nafion).[7,17,18] The fabrication of a modified GCE is time-consuming and costly due to the additional preparation steps. In addition, Nafion is not electrochemically active for cholesterol and H_2O_2 detection and blocks the available electrocatalytic sites.[19] Furthermore, the active material of a modified CGE may also be prone to the detachment and dissolution in the electrolyte, which limit the long-term stability of the sensor.[20,21] Hence, the selection of electrode material plays a critical role in nonenzymatic electrochemical sensors. The physicochemical properties of the substrate material have an immense influence on the electrochemical performance of the biosensors. Recently, anodic TNT arrays have attracted considerable attention due to their strong adhesion with the Ti substrate, chemical stability, low cost, and excellent biocompatibility.[22−26] The self-organized, highly ordered, and vertically aligned nanostructures of anodic TNTs with high surface area are very useful for loading other electrochemically active materials, leading to hybrid nanostructures. Furthermore, a Schottky-type contact is formed between the TNTs and Ti substrate, which facilitates the transport of electrons from the electrode surface to the metal substrate.

Despite so much promise, the biosensing performance of TNTs suffers due to their large band gap, which impedes the electron transfer efficiency; hence, TNTs showed a poor response as a biosensor. Appropriate surface modifications of TNTs with low band gap semiconductor QDs can be helpful to minimize the localized surface trap states, resulting in the increased electron transfer efficiency.[8,27] Besides, the good size tenability, improved surface capping chemistry, high quantum yield, and broad absorption of QDs make them a promising material in biosensing applications.[8,28−31] Among various QDs, CdS with band gap of about 2.4 eV has been reported as an active fluorescent probe and photoelectrochemical material for the detection of biological analytes.[30−32] Most of the CdS QDs-based studies used their optical properties,[8,23,30−35] and very little efforts have been made to utilize their electrochemical properties[28,29,36,37] for exploring the sensing aspects of different biological molecules. Moreover, these QDs need a supporting material that enables them to be homogeneously dispersed and stable. Therefore, choosing an appropriate material with a favorable morphology as a matrix is critical. In our case, we have used TNTs as a matrix material, utilizing their higher surface area for CdS QD decoration. Moreover, introducing the noble metal supported catalyst, e.g., Au NPs film, on the electrode surface can greatly increase the stability of CdS QDs and effectively contributes to the electronic conductivity of the biosensor. The higher biocompatibility, enhanced chemical stability, enhanced antipoisoning characteristic, and ability to bind with many biological ligands (proteins) of Au NPs make them a promising material in biosensing. In previous reports, Dhyani and co-workers have established an enzymatic cholesterol biosensor based on polyaniline and CdS QD nanocomposites deposited on an indium tin oxide (ITO) coated glass plate.[38] Zhong and his group fabricated a hemoglobin-immobilized CdS:Mn NPs-based biosensor for the detection of H_2O_2.[36] Y. Huang et al. reported an enzyme-based glucose biosensor modified with CdS NPs.[37] Furthermore, an enzyme-free biosensor using a bifunctional Ni/CdS/TiO_2 core−shell nanowire electrode has been reported with a sensitivity of ∼1136.67 μA mM^{-1} cm^{-2} for the reliable detection of glucose.[27]

A novel approach for the fabrication of cost-effective nonenzymatic biosensors for sensing dual analytes, which are electrochemically active on different onset potentials, on the same electrode material has been achieved. Herein, we report a sensitive voltage-switchable enzyme-free electrochemical cholesterol and H_2O_2 dual biosensor based on Au NPs/CdS QDs decorated TNTs. Au/CdS QDs/TNTs show a redox peak at −1.2 V for cholesterol and −0.55 V for H_2O_2 reduction. These potentials were further utilized to observed the response current of the electrodes for analyte detection in amperometric studies. Both cholesterol and H_2O_2 are electrochemically active on a completely different potential while using a single-electrode system (Au/CdS/TNTs). By switching the applied potential between two different values, the sensing behavior of the biosensor could be specified for any one of the target analytes. The hybrid electrode exhibited an excellent sensitivity with an enhanced electron transfer rate due to the proper band gap alignment of the active materials. Au NPs and CdS QDs provide channels on the surface of TNTs for the redox species to transport from the redox center of the analyte toward the electrode. In addition, the low redox potential of the electrode may reduce the interference to cholesterol and H_2O_2 in the presence of common interfering species and increases the practicality of the biosensor for clinical sample analysis. The proposed biosensor can provide a general consideration for the design of a nonenzymatic electrochemical sensor to detect other biological molecules.

MATERIALS AND METHODS

Titanium (Ti) foils of 0.1 mm thickness and 99.6% purity were purchased from Goodfellow, England. Ethylene glycol (EG, 99.9% purity), ammonium fluoride (NH_4F), cadmium chloride ($CdCl_2$, 99.99%), and sodium sulfide (Na_2S, 99.5%) were obtained from Sigma Aldrich, USA. Other chemicals including cholesterol, urea, ascorbic acid (AA), glucose, H_2O_2, and L-cysteine were supplied by Sinopharm Chemical Reagent Co. Ltd., P.R. China. All the chemicals were of analytical grade and used in the as-received form without

https://dx.doi.org/10.1021/acsami.0c19979
ACS Appl. Mater. Interfaces 2021, 13, 3653−3668

further purification. Deionized (DI) water was used as per the requirement of the synthesis and sensing experiments.

Fabrication of the Au/CdS QDs/TNTs Biosensing Platforms. The Au/CdS QDs/TNTs electrode was prepared using a four-step process as presented in Scheme 1. This process contains (a) the formation of TNTs on the Ti substrate via anodization (b) followed by the deposition of CdS QDs through the chemical bath deposition method. In the third step, (c) a thin layer of Au was deposited on CdS/TNTs, (d) which was then annealed in an Ar atmosphere to convert the thin sputtered Au layer into a layer of Au NPs on the top surface as well as somewhat inside the nanotubes. The details of the fabrication process are given as follows.

Scheme 1. Schematic Representation of the Fabrication Process of the Au/CdS QDS/TNTs Biosensing Platform

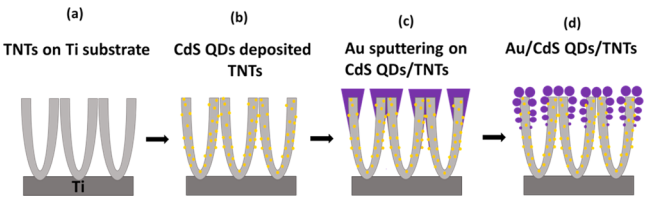

Anodization of Ti. Prior to the anodization process, the Ti foils were cleaned by sonicating in acetone, ethanol, and DI water successively for 15 min each followed by drying in a nitrogen (N_2) stream. Anodization was performed using a high-voltage potentiostat (Jaissle IMP 88 PC, Germany) in a two-electrode configuration with the Ti foil as the working electrode and the Pt foil as the counter electrode. Self-organized, highly ordered, and vertically aligned TNTs were fabricated by anodization of the Ti foils in an EG-based electrolyte using a two-step anodization that is useful to obtain TNTs with a complete open-top morphology. In the first step, the Ti foil was anodized in 40 mL of the EG electrolyte containing 0.25 wt% NH_4F and 5 wt % DI water at 50 V for 4 h. These TNTs attached to the Ti foil were then removed by sonication in DI water for 15 min. As a result, a honeycomb-like patterned morphology was produced on the surface of the Ti foil. The patterned morphology was subsequently used for the second-step anodization in a fresh electrolyte (of the same composition as that used in the first step) under identical conditions (Scheme 1a). After the second-step anodization, the samples were washed with ethanol and dried in a N_2 stream. The resulting amorphous TNTs were annealed in air at 450 °C for 2 h with the same heating and cooling rates (3 °C/min) to obtain the anatase phase.

Decoration of TNTs with CdS QDs. The ultrasonication-assisted successive ion layer adsorption and reaction (SILAR) method was employed for decorating TNTs with CdS QDs (Scheme 1b). This method is very beneficial for the homogeneous and uniform deposition of QDs inside the TNTs. The annealed TNTs were sequentially immersed in four different beakers for 1 min in each beaker during the sonication process at room temperature. The first beaker contained a 0.05 M $CdCl_2$ aqueous solution, the next one contained a 0.05 M Na_2S aqueous solution, and the remaining two consisted of DI water for washing. The excess amount of the precursors was removed by washing with DI water after each step. This four-step process (soaking and rinsing) is considered as one cycle. This process was repeated for 3, 6, 9, and 12 cycles to increase the density of CdS QDs on TNTs, producing strong yellowish samples. The samples were named as CdS(3) QDs/TNTs, CdS(6) QDs/TNTs, CdS(9) QDs/TNTs, and CdS(12) QDs/TNTs corresponding to the number of cycles used in the SILAR decoration process.

Deposition of the Au Layer on CdS QDs/TNTs. To deposit a layer of Au on the top surface of the CdS QDs/TNTs electrode (Scheme 1c), the plasma sputter deposition (EM SCD500, Leica) technique was used. A pure Au metallic target (Hauner Metallische Werkstoffe) was utilized as a source material. The sputtering was carried out at 10^{-2} mbar of argon (Ar) by applying a current of 15 mA. A Au film with different thicknesses (5, 10, 20, and 30 nm) was deposited on the CdS QDs/TNTs electrode. The thickness of the sputtered Au was controlled with an automated quartz crystal film-thickness monitor.

Conversion of the Sputtered Au Layer via Thermal Dewetting. The Au film was annealed at 400 °C in an Ar atmosphere for 1 h to convert the sputtered Au layer into a layer of Au NPs (Scheme 1d). The conversion of the thin Au layer into Au NPs is ascribed to the thermal dewetting, which is the breaking of the continuous metal film into islands/beads to minimize the surface energy of the metal and metal oxide and at the interface of the metal and metal oxide. The Au NPs deposited on CdS QDs/TNTs in various layer thicknesses were named as Au(5)/CdS(6) QDs/TNTs, Au(10)/CdS(6) QDs/TNTs, Au(20)/CdS(6) QDs/TNTs, and Au(30)/CdS(6) QDs/TNTs. For comparison, a sample of Au/TNTs with a 10 nm thick sputtered Au layer was also annealed at 400 °C under similar conditions.

Characterization. The structural morphology of the samples was studied with the help of a field emission scanning electron microscope (FESEM, Hitachi S-4800, Japan). The cross-sectional FESEM images were collected for the mechanically cracked samples. A high-resolution transmission electron microscope (HRTEM, Tecnai G2

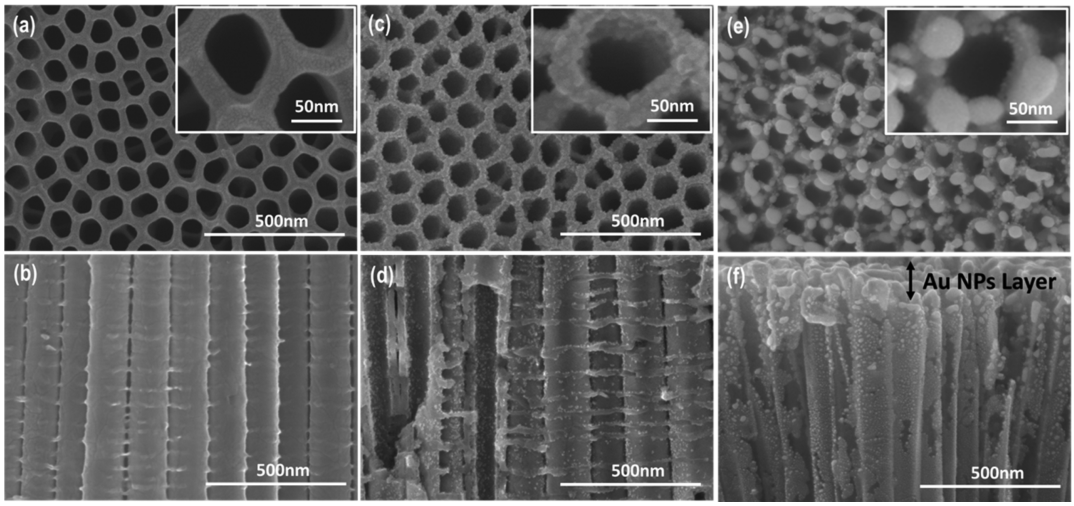

Figure 1. SEM images showing the top view and cross-sectional view of (a, b) pristine TNTs, (c, d) CdS(9) QDs/TNTs, and (e, f) Au(10)/CdS(9) QDs/TNTs, respectively. Insets a, c, and e show the top view at high magnification.

https://dx.doi.org/10.1021/acsami.0c19979
ACS Appl. Mater. Interfaces 2021, 13, 3653−3668

F20 S-Twin, FEI, USA) was used for the characterization of the samples. X-ray photoelectron spectroscopy (XPS, PHI 5600, USA) and X-ray diffraction (XRD, X'pert Philips PMD, Cu Kα 1.54056 Å) were employed to determine the chemical state and crystal structure of the samples, respectively. Electrochemical impedance spectroscopy was performed using Zahner (IM6ex, Germany). The electrochemical measurements including cyclic voltammetry and amperometry were carried out in 0.1 M phosphate buffer solution (PBS) at pH 7.0 using an electrochemical workstation (CHI660C, China) with a three-electrode configuration (where Ag/AgCl serves as a the reference and Pt as the counter electrode). For cholesterol sensing, 0.9 g of cholesterol was first dissolved in 2 mL of 2-propanol to make the solution, which was then diluted to 50 mM in 0.1 M PBS at pH 7.0 to make the stock solution. This stock solution was further diluted in PBS as per the requirement. For H_2O_2, a stock solution of 15 mM was prepared for the electrochemical measurements.

RESULTS AND DISCUSSION

Scanning Electron Microscopy. Figure 1a–f shows the SEM images of the pristine TNTs, CdS(9) QDs/TNTs, and Au(10)/CdS(9) QDs/TNTs samples. It is evident from the top view of the pristine TNTs (Figure 1a) that self-organized and highly ordered nanotubes were formed that are covered by a thin nanoporous layer with a clear open-top morphology (Figure S1a). A thin nanoporous layer is usually formed on the top surface of TNTs after the second-step anodization of the honeycomb-like patterned morphology (which was achieved after removing the TNT film after the primary anodization step). The average diameter of TNTs was about 100 nm with a wall thickness of ~15 nm (inset of Figure 1a). Figure 1b represents the cross-sectional image of the pristine TNTs that shows the formation of ripples on the walls of the nanotubes. This can be attributed to the water content in the electrolyte. A uniform and homogeneous deposition of CdS QDs on the top as well as on the outer and inner walls of TNTs has been observed after decoration using the modified SILAR method (Figure 1c,d). Decoration of TNTs with CdS QDs using the conventional SILAR method (Figure S1b) results in the clogging of the nanotubes' opening. In the modified form, the ultrasonication enhances the penetration of the Cd and S ions inside the nanotubes where they react with each other without clogging the top of the nanotube (inset of Figure 1c). It can be seen from Figure 1d that CdS QDs are deposited on both side walls (inner as well as outer walls) of the nanotubes throughout their entire length. This may also enhance the electrochemical response of the CdS QDs /TNTs electrode in biosensing. In addition, the SEM top view images for different deposition cycles of CdS QDs are presented in Figure S2. It can be seen that the density of CdS QDs increases by increasing the number of cycles from 3 to 9 (Figure S2a–c). A further increase in the deposition cycles to 12 (Figure S2d) results in the agglomeration of CdS QDs at the top, leading to the blockage of the tube's opening. Figure 1e,f shows the top and cross-sectional SEM images of the Au NPs layer deposited on CdS(9) QDs/TNTs. A homogenous distribution of the dewetted Au NPs is observed (Figure 1e) over a larger area of the electrode surface. An optimized sputtered Au layer thickness of 10 nm was used, which prevents the clogging of the nanotubes' opening by Au NPs after thermal dewetting.

The average size of the Au NPs and their penetration depth inside the nanotubes depends on the initial thickness of the sputtered Au layer and the sputtering angle. We have opted for a deep sputtering angle such that the Au NPs can penetrate inside the nanotubes. Figure S3 (in the Supporting Information) shows the schematic illustration of the effect of the sputtered Au layer thickness on the CdS QDs/TNTs electrode. This description is based on the results obtained from the SEM images as shown in Figure S4a–h. Figures S3a and S4a,b depict that when the layer thickness of the sputtered Au is 5 nm, the thermal dewetting results in a uniform distribution of Au NPs at the tube tops (Figure S4a). The cross-sectional SEM image in Figure S4b reveals that a comparatively bigger Au NP lies at the rim of the tubes' opening, whereas the size reduces along the length of TNTs, which can be due to the low penetration depth of the Au sputtered layer along with the gradually decreased layer thickness across the tube length (Figure S3a). Due to this reason, the Au NPs are limited to the top surface regions of the tubes. The thermal dewetting of the 5 nm thick Au layer induces a wide range of particle size distribution on the tube walls near the top region of the TNTs. The average particle size of Au NPs has been estimated from near the top region of the TNTs as indicated by a square (Figure S4b). An average particle size of 14 nm is obtained for the specified region. However, the particle size of Au NPs may vary depending on the region under study. Figures S3b–d and S4c–h show that the particle size and penetration depth of Au NPs increase when increasing the thickness of the Au layer to 10, 20, and 30 nm. The average particle size for the 10, 20, and 30 nm dewetted Au layer is about 20, 37, and 72 nm, respectively (Figure S4d,f,h). These results further show that the optimum layer thickness is 10 nm because for higher layer thicknesses of sputtered Au after thermal treatment, large Au islands are formed at the rim of the TNTs (Figure S4e,g), which close the tube opening and reduce the synergistic effect of CdS QDs and TNTs due to a shading effect. For comparison, the TNTs decorated with Au NPs sputtered with the 10 nm Au layer thickness are shown in Figure S5a,b.

Transmission Electron Microscopy. Figure 2a,b shows the TEM images of TNTs decorated with CdS QDs and Au NPs formed by the thermal annealing of the 10 nm sputtered Au layer at the top of the CdS QDs/TNTs. The image shows that the CdS QDs are uniformly deposited over all the tube walls as marked by the arrows in Figure 2b. The deposition of the Au NPs from the dewetted Au layer is evident from the tube walls, which become significantly coarser after the sputtering and dewetting of the Au layer; an apparent decrease in the tube diameter at the top region of the nanotubes is also

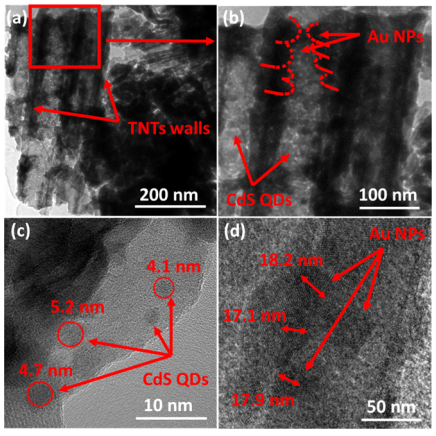

Figure 2. (a, b) TEM images of Au/CdS QDS/TNTs. HRTEM images of (c) CdS QDs/TNTs and (d) Au/TNTs.

https://dx.doi.org/10.1021/acsami.0c19979
ACS Appl. Mater. Interfaces 2021, 13, 3653–3668

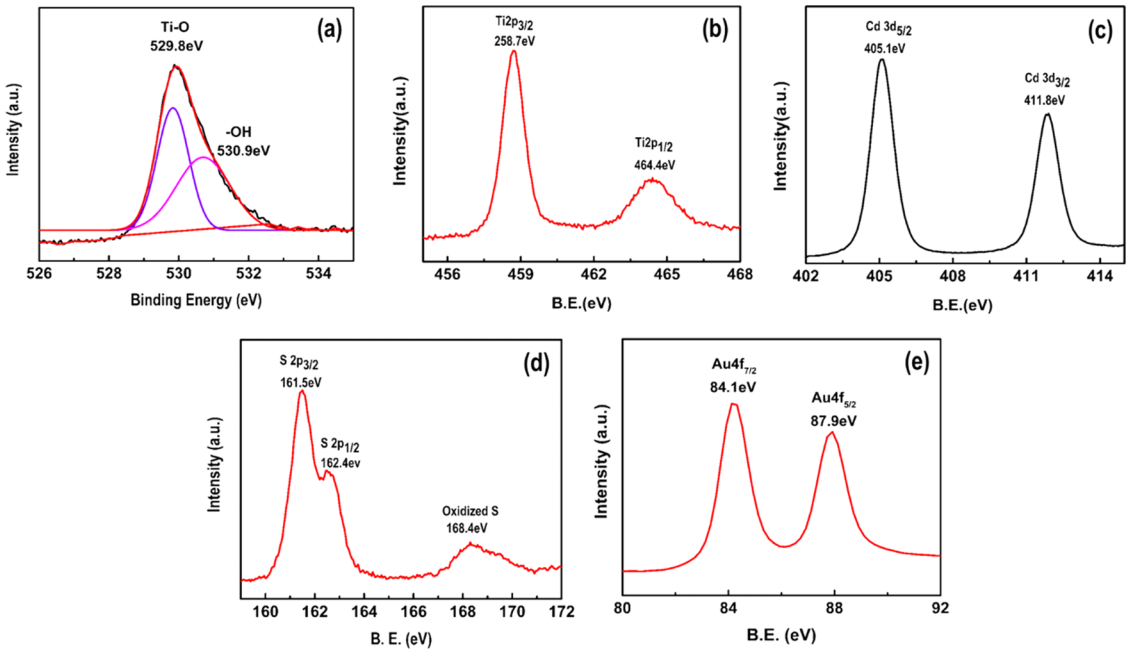

Figure 3. High-resolution XPS spectra of Au(10)/CdS(9) QDs/TNTs: (a) O1s, (b) Ti2p, (c) Cd3d, (d) S2p, and (e) Au4f.

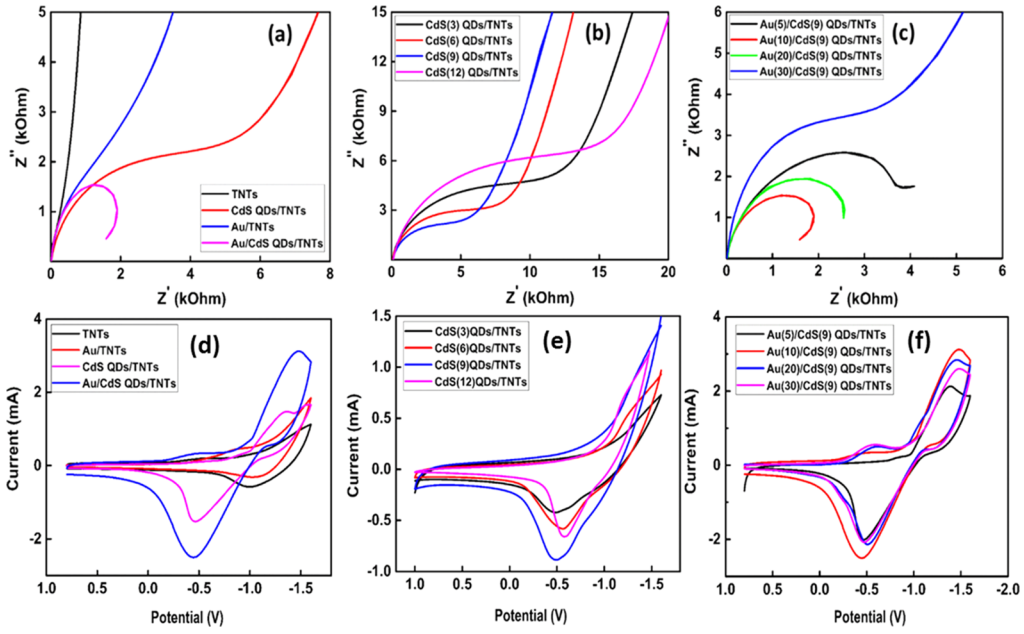

Figure 4. Electrochemical impedance spectroscopy (EIS) spectra (a) at different stages of electrode fabrication, (b) at different decoration cycles of CdS QDs on TNTs, and (c) for different layer thicknesses of Au NPs on the CdS(9) QDs/TNTs electrode. Cyclic voltammograms (d) of different electrode configurations in 0.1 M PBS obtained at 50 mV s^{-1}. CV scans of TNTs (e) decorated with CdS QDs for different deposition cycles and (f) of CdS QDs/TNTs for different layer thicknesses of the Au NPs film.

observed. These results reveal that the Au nanoparticles are only confined to the upper portion of the TNTs and are represented by the dotted semicircles for clarity in Figure 2b. This fact can be explained by the lower penetration depth of the sputtered Au layer that induces the Au NPs through thermal dewetting. These findings were further supported by the cross-sectional SEM images (Figure 1e,f) that show that most of the Au NPs are confined at the top regions of the nanotubes. After Au sputtering, a thick and uniform layer has been deposited at the top surface of the nanotubes, while the thickness of the layer was gradually decreased along the tube length. The thermal dewetting of this layer leads to the formation of bigger Au NPs at the crown positions of TNTs, whereas the size of these Au NPs decreases along the tube length. By further exploring the nanotubes along the length, the Au NPs disappear and only CdS QDS are present, which are previously deposited uniformly over all the tube length as confirmed by SEM (Figure 1d).

To further investigate the particle size, the HRTEM images of CdS(9) QDs/TNTs and Au/TNTs system are shown in Figure 2c and d, respectively. Figure2c shows that the average size of the CdS QDS is 4.6 nm. Figure 2d depicts that after the

https://dx.doi.org/10.1021/acsami.0c19979
ACS Appl. Mater. Interfaces 2021, 13, 3653−3668

thermal treatment of the 10 nm Au sputtered layer, an average particle size of 17.3 nm is obtained for Au NPs on TNTs in close proximity to the top surface. These finding are in line with the SEM results from Figure S4d that show that the Au NPs exhibit an average size of 20 nm. The particle size of CdS QDs via SEM could not be estimated due to their smaller size.

X-ray Photoelectron Spectroscopy. To investigate the chemical composition and oxidation states, XPS measurements were performed for Au/CdS QDs/TNTs. Figure 3 shows the high-resolution XPS spectra of O1s, Ti2p, Cd3d, S2p, and Au4f. The O1s spectrum (Figure 3a) exhibits a strong peak at ∼529.8 eV that can be assigned to the anionic oxygen in the TiO_2 lattice. In addition, a small peak located at about 530.9 eV that corresponds to the hydroxyl species is also present.[39] In Figure 3b, the peaks located at the binding energies of around 458.7 and 464.4 eV can be assigned to $Ti2p_{3/2}$ and $Ti2p_{1/2}$, respectively. These states demonstrate the presence of the Ti^{4+} states within the sample.[40] Figure 3c shows the XPS core-level spectra of Cd3d. The binding energy peaks of $Cd3d_{3/2}$ and $Cd3d_{5/2}$ are located at ∼411.8 and 405.1 eV, respectively.[39,41,42] The binding energy difference between $Cd3d_{3/2}$ and $Cd3d_{5/2}$ is 6.7 eV, which is the characteristic of the Cd^{2+} state.[39] The core-level XPS spectrum of S2p is shown in Figure 3d. The peak position at about 161.5 and 162.4 eV could be assigned to the $S2p_{3/2}$ and $S2p_{1/2}$ states of the S^{2-} anion.[41,42] These results further confirm the formation of CdS during the decoration process via the modified SILAR method. The high-resolution XPS spectra of Au4f are shown in Figure 3e; it is seen that two peaks are located at the binding energies of around 84.1 and 87.9 eV that are assigned to the $4f_{7/2}$ and $4f_{5/2}$ peaks of Au NPs, respectively.[43] The binding energies of the peak show the presence of a pure metallic phase of Au NPs on the surface of the CdS QDs/TNTs electrode.

■ ELECTROCHEMICAL MEASUREMENTS

Electrochemical Impedance Spectroscopy. Figure 4a shows the Nyquist plots of the pristine TNTs, CdS QDs/TNTs, Au/TNTs, and Au/CdS QDs/TNTs electrodes that were recorded at a bias voltage of 0.3 V. The charge transfer resistance at the electrode/electrolyte interface can be estimated from the diameter of the semicircle of the Nyquist plot at high frequencies. The pristine TNTs exhibited a large semicircle at high frequencies; however, the area of the semicircle abruptly decreased by incorporating CdS QDs within the system. The area of the semicircles decreases by increasing the number of the CdS QDs deposition cycles (Figure 4b). This may be attributed to the fact that the incorporation of CdS QDs into TNTs leads to the higher surface area along with increasing the active sites for the electrochemical reactions. This can play a role in enhancing the electrocatalytic performance of the electrode, as the band edge position of CdS with respect to TiO_2 favors the fast electron transport from the electrolyte via the conduction band (CB) of CdS to the CB of TiO_2. It is important to mention that for the sample CdS(12) QDs/TNTs, the high-frequency semicircle was not observed. This may be attributed to the increased capacitive effects due to the clogging of CdS QDs at the nanotubes' opening as confirmed from the SEM results (Figure S2d). The clogging closes the tube opening; as a result, the area of TNTs exposed to the electrolyte also decreases, which leads to the poor electron transfer due to the higher interface capacitance.[44] Therefore, CdS(9) QDs/TNTs were further used for the deposition of the Au NPs layer. In case of the Au/CdS QDs/TNTs electrode, the diameter of the semicircle was greatly reduced and a higher electrochemical activity of the hybrid electrode was observed (Figure 4a). The Au NPs layer introduced more active sites at the top surface of the electrode and the fermi level of Au NPs aligned with the CB of CdS QDs, which significantly increases the electron transfer rate at the interface of the electrode. The EIS of the Au/TNTs electrode was also presented for comparison. Figure 4c shows the EIS for different sputtered Au film thicknesses on the CdS QDs/TNTs electrode after thermal treatment, which depicts the higher electrochemical response for the Au(10)/CdS(9) QDs/TNTs electrode configuration.

Cyclic Voltammetry Analysis of the Different Electrode Configurations. The electrochemical activities of the pristine TNTs, CdS QDs/TNTs, Au/TNTs, and Au/CdS QDs/TNTs were investigated in 40 mL of 0.1 M PBS with pH 7.0 using cyclic voltammetry (CV). Anodization results in the direct growth of TNTs on the Ti metal substrate, leading to a back-supported oxide electrode that can be used directly for the electrochemical measurements. Therefore, the requirement of using conductive polymer binders or adhesive is eliminated. Figure 4d shows the CV (recorded at a scan rate of 50 mV s^{-1}) for all samples. For the pristine TNTs, no obvious oxidation or reduction peaks were observed. The CV of Ar annealed CdS QDs/TNTs electrode shows a rapid increase in the current response with a pair of well-defined oxidation (−0.5 V) and reduction peaks (−1.2 V) that corresponds to the enhanced electrochemical activity of the electrode introduced by CdS QDs. In case of the Au/CdS QDs/TNTs electrode, an about 3 times increase in the oxidation and reduction peak currents with a slight shift in the peak positions was observed. These results indicate that the incorporation of the Au NPs layer on CdS QDs decorated TNTs enhanced the electrochemical activity for the required redox reaction that can be ascribed to the increased surface area and availability of additional active sites at the surface of the electrode. The CV of Au/TNTs electrode is also presented for comparison. The deposition of the Au NPs on TNTs significantly increases the current and introduces a reduction peak at −0.7 V. The effect of the CdS QDs deposition cycles on the redoxpeak current was also measured by CV as presented in Figure 4e. It was found that by increasing the deposition cycles, the oxidation and reduction current increases due to the availability of more active sites for the redox reaction. However, when the number of deposition cycles was increased to 12, a rapid decrease in the oxidation and reduction current was observed. This abrupt decrease can be ascribed to the deficiency of the required active sites due to the clogging of QDs at the tube opening as shown in Figure S2d. This agglomeration prevents the penetration of the electrolyte inside the TNTs and in turn hinders the available active sites. Additionally, a careful optimization of the thickness of the thermally dewetted sputtered Au layer (Au NPs) on CdS QDs/TNTs was carried out by measuring CV for 5, 10, 20, and 30 nm as shown in Figure 4f. Besides the introduction of an additional peak (at −0.5 V due to the redox reaction of Au NPs) for higher film thicknesses (10, 20, and 30 nm), a higher current response was observed for the Au NPs layer obtained from the 10 nm sputtered Au layer. This can be attributed to the uniform distribution of Au NPs at the crown positions of TNTs without blocking the tubes' opening. Thus, Au NPs decorated CdS QDs/TNTs achieved from dewetting of the 10 nm layer

https://dx.doi.org/10.1021/acsami.0c19979
ACS Appl. Mater. Interfaces 2021, 13, 3653−3668

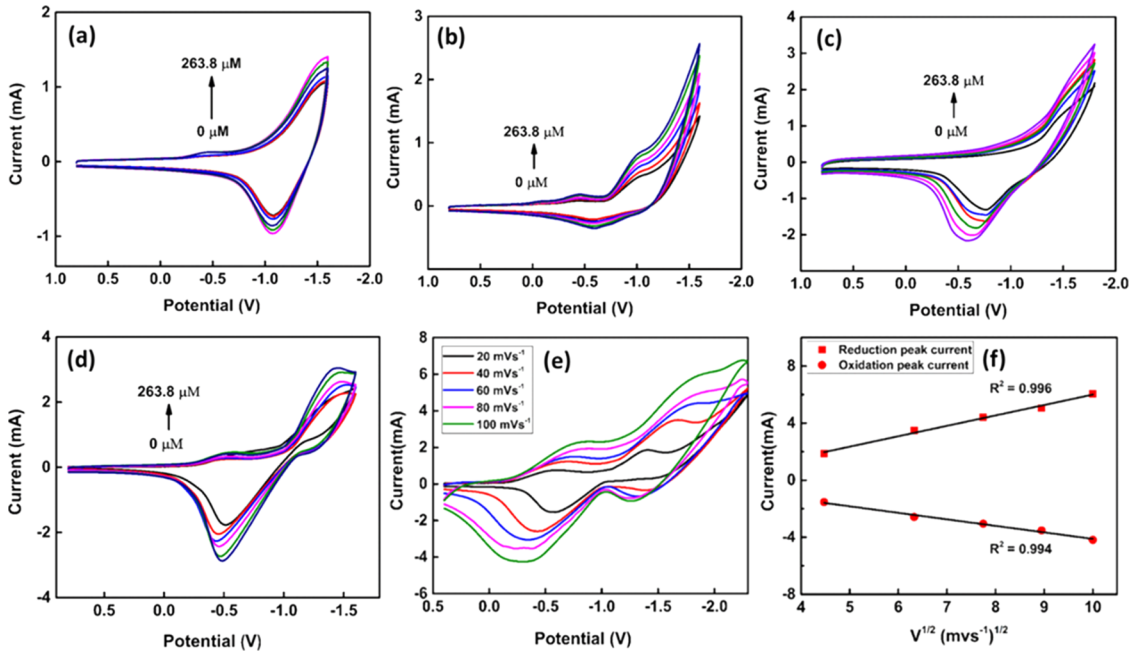

Figure 5. CV scans with the addition of different concentrations of cholesterol for (a) TNTs, (b) Au/TNTs, (c) CdS QDs/TNTs, and (d) Au/CdS QDs/TNTs. (e) CV of Au/CdS QDs/TNTs as a function of scan rate (20−140 mV s^{-1}) with 475 μM cholesterol in 0.1 M PBS. (f) Linear fitting of redox peak currents as a function of the square root of the scan rate.

thickness of sputtered Au were further used for the detailed investigation of the electrochemical properties.

Electrochemical Detection of Cholesterol on Au/CdS QDs/TNTs. Figure 5a−d shows the CV of TNTs, Au/TNTs, CdS QDs/TNTs, and Au/CdS QDs/TNTs with the addition of different concentrations of cholesterol in the electrolyte. The CV of TNTs (Figure 5a) did not show any predominant redox peaks without any cholesterol concentration. Initially, by introducing the cholesterol within the electrolyte, a very small increase in the oxidation current is observed at lower concentrations; however, this increase becomes significant for higher cholesterol concentrations. These results suggest that the TNTs are electrochemically active at higher cholesterol concentrations. The CV of Au/TNTs (Figure 5b) shows an increase in the redox peak current by increasing the cholesterol concentrations. The deposited Au NPs on TNTs increase the surface area of the electrode, which increases the electrochemically active reaction sites for the oxidation process. The Au NPs serve as a co-catalyst with synergistic effects and act as an electron reservoir that is helpful to attain the detection of cholesterol at lower concentrations. The redox peak current for Au/TNTs further increases by increasing the cholesterol concentration. For CdS QDs/TNTs (Figure 5c), the well-defined redox peak is observed without any cholesterol concentration, while the redox peak intensity increases with the successive addition of cholesterol within the electrolyte. This can be attributed to the increased surface area of the electrode as well as the combined synergistic effect of CdS QDs and TNTs. CdS is an n-type material and has suitable band edge positions in reference to the standard redox potentials, which assist to initiate the novel redox reactions for cholesterol oxidation (cholesterol auto-oxidation process). It also facilitates the rapid charge transfer from the redox centers of the redox species via TNTs toward the back contact Ti substrate. The ternary electrode Au/CdS/TNTs utilize the combined synergistic effects of TNTs, CdS, and Au for a highly sensitive cholesterol detection (Figure 5d). The redox current significantly increases by increasing the cholesterol over a wide range of concentrations. This enhancement can be attributed to two factors. One is related to the lowering of the redox potential of the electrode by incorporating CdS QDs, and the other is the availability of a large number of catalytically active electrons centers due to the gold layer.

The effect of the potential scan rate on the oxidation and reduction peak currents in the presence of cholesterol was also investigated and displayed in Figure 5e. It can be seen that the oxidation and reduction currents for cholesterol increase by increasing the scan rate from 20 to 100 mV s^{-1}. The linear fitting of the redox peak current is presented in Figure 5f, which implies its proportionality on the root mean square of the scan rate, indicating the diffusion-controlled process of the cholesterol oxidation at the surface of the electrode.[28,38]

To evaluate the effect of the ambient light on the electrochemical performance of the biosensor, cyclic voltammetry for all electrode configurations was performed under completely dark conditions for cholesterol detection. All previous experiments were performed in ambient light (room lights), while the following dark experiments were performed within a black box placed in a dark room. The comparison of the CV measured under the ambient light and dark conditions for pristine TNTs, Au/TNTs, CdS/TNTs, and Au/CdS/TNTs is presented in the Supporting Information (Figure S6a−d).

The CV of pristine TNTs (Figure S6a), Au/TNTs (Figure S6b), CdS QDs/TNTs (Figure S6c), and Au/CdS QDs/TNTs (Figure S6d) under the dark and ambient light conditions shows the close contact between the redox peak current values without any significant difference in the redox peak positions. For each electrode, an almost equivalent increase in the redox peak currents is observed with the addition of 211.1 μM cholesterol under both conditions. Moreover, the results depict the higher redox current for the

https://dx.doi.org/10.1021/acsami.0c19979
ACS Appl. Mater. Interfaces 2021, 13, 3653−3668

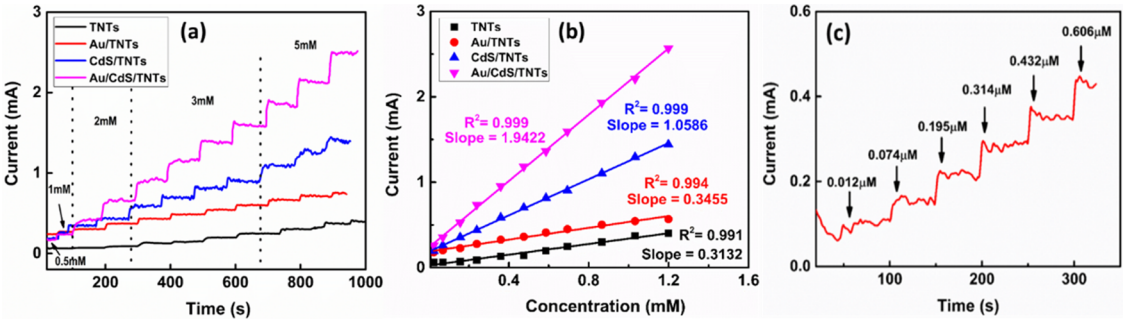

Figure 6. Amperometric response of the pristine TNTs, Au/TNTs, CdS QDs/TNTs, and Au/CdS QDs/TNTs at −1.2 V upon the successive addition of cholesterol in 40 mL of 0.1 M PBS at pH 7.0; (b) corresponding linear calibration curve of cholesterol concentration. (c) Amperometric response of the electrode toward a lower concentration of cholesterol.

Table 1. Comparison of Au/CdS QDs/TNTs Cholesterol Biosensor with Other Electrode Systems

s. no.	electrode materials	LOD	sensitivity (μA mM^{-1} cm^{-2})	response time (s)	LDR (mM)	reference
1.	1D porous tubular Ag/GCE	0.18 mM	0.7		28−0.33	47
2.	Au-/nPts	15 μM	226.2		0.015−5	48
3.	Cu_2S-NRs/CRIE	0.1 μM	62.5 μA mM^{-1}	3	0.01−6.8	52
4.	Pt-NP/CNT	0.0028 mM	8.7		0.005−10	49
5.	CNT	0.01708 μM	1531	6		53
6.	Au/CdS QDs/TNTs	0.012 μM	10,790	1	0.024−1.2	present work

Au/CdS QDs/TNTs system as compared to CdS QDs/TNTs, Au/TNTs, and TNTs in both the ambient and dark conditions. These results shows that in spite of the photoactive nature of the electrode functional materials, the ambient light did not significantly influence the electrochemical response of the electrodes as the light is highly dispersed and the intensity of the light is not significant for the photoelectrochemical generation of an electron hole pair that is considered a key factor for the photoassisted redox reactions. In the literature, it is verified that the sensing aspects of photoelectrochemical sensors are dependent on the intensity of the light source.[45,46] Therefore, it is suggested that the electrochemical generation of the redox species (by applying a voltage) is the leading phenomenon for the higher electrochemical activity of the biosensor.

The amperometric studies of the pristine TNTs, CdS QDs/TNTs, Au/TNTs, and Au/CdS QDs/TNTs samples were performed in 40 mL of 0.1 M PBS with pH 7.0 in response to the successive addition of different concentrations of cholesterol under vigorous stirring conditions (Figure 6a). During these measurements, an optimized potential of ∼−1.2 V was applied, which was found to be more negative than the previously reported values in nonenzymatic sensors.[47−49] This factor can strongly improve the selectivity of the biosensor because most of the interfering species within the human blood serum such as urea and AA are electrochemically active at positive potentials.[50,51] Figure 6a presents the amperometric response of the pristine as well as hybrid samples. Both the pristine and CdS QDs/TNTs samples achieved about 95% of the steady-state current within less than 8 and 3 s in response to the addition of each concentration of cholesterol, respectively. The response current was further increased, and an improvement in the response time (1 s) was observed for the Au NPs decorated CdS QDs/TNTs.

Figure 6b shows the calibration curves for all samples, indicating the linear dependency of oxidation current on cholesterol concentration. This calibration curve was derived from the amperometry response by taking into account the dilution factor (due to 40 mL of the electrolyte solution) for cholesterol concentration. The sensitivity of Au/CdS QDs/TNTs (∼10,790 μA mM^{-1} cm^{-2}) was about 2 times higher than that of CdS QDs/TNTs (∼5881 μA mM^{-1} cm^{-2}), while the sensitivity of CdS QDs/TNTs was about 3- and 3.5-fold higher than that of Au/TNTs (1994 μA mM^{-1} cm^{-2}) and pristine TNTs (1740 μA mM^{-1} cm^{-2}), respectively, as shown in Table S1. Moreover, the Au/CdS QDs/TNTs electrode possesses a low detection limit (LOD) (∼0.012 μM) and a wide linear range (0.024−1.2 mM) for cholesterol detection compared to the CdS QDs/TNTs, Au/TNTs, and pristine TNTs. The LOD was determined by establishing the lowest concentration of the cholesterol at which an increase in the current above the baseline is reliably and clearly obtained as shown in Figure 6c.

The proposed electrode exhibited a good performance in terms of sensitivity, linearity, detection limit, and response time when compared with other nanostructure-based enzyme-free cholesterol sensors composed of other electrode materials. Yi Jae Lee and Jae Yeong Park have developed a macroporous Au-/nPts electrode by electroplating Pt NPs on a macroporous structured Au electrode for the nonenzymatic detection of cholesterol and achieved a sensitivity of 226.2 μA mM^{-1} cm^{-2}.[48] Rong Ji and his group have fabricated a roselike copper(I) sulfide nanostructure (Cu_2S NRS) synthesized on a copper rod and utilized for enzyme-free cholesterol detection. They had found a sensitivity of 62.5 μA mM^{-1}.[52] Mitali Saha and Soma Das have obtained carbon nanotubes from coconut oil and attained a sensitivity of 1531 μA mM^{-1} cm^{-2}.[53] However, in our case, the Au/CdS/TNTs electrode shows a maximum sensitivity of 10,790 μA mM^{-1} cm^{-2} for nonenzymatic cholesterol detection, which is much higher than the values reported in the literature for cholesterol sensors as summarized in Table 1. To the best of our knowledge, this sensitivity value is the highest among those reported in the literature for cholesterol sensors.

To further elaborate the influence of ambient light on the electrochemical response of the biosensor, the amperometric

https://dx.doi.org/10.1021/acsami.0c19979
ACS Appl. Mater. Interfaces 2021, 13, 3653−3668

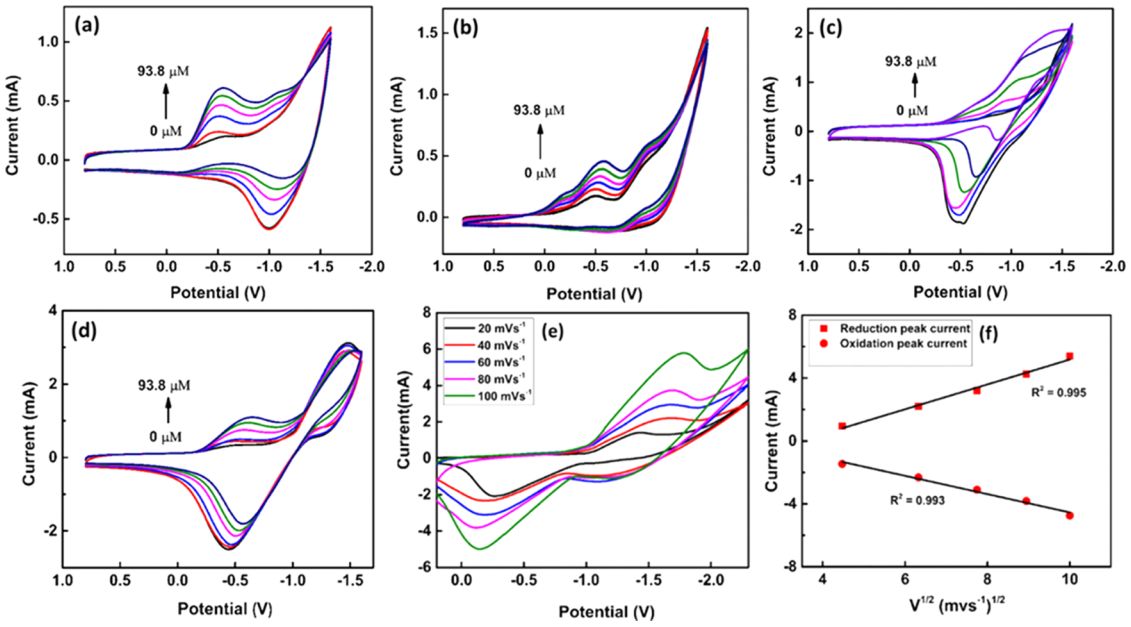

Figure 7. CV scans with the addition of different concentrations of H_2O_2 for (a) TNTs, (b) Au/TNTs, (c) CdS QDs/TNTs, and (d) Au/CdS QDs/TNTs. (e) CV of Au/CdS QDs/TNTs as a function of scan rate (20−140 mV s^{-1}) with 131.3 μM H_2O_2 in 0.1 M PBS. (f) Linear fitting of redox peak currents as a function of the square root of the scan rate.

studies were carried out under completely dark conditions in a dark room. The amperometric data as presented in Figure S7a show a linear increase in the response current with the addition of different cholesterol concentrations, where a higher response current is observed for the Au/CdS QDs/TNTs composite electrode as compared to CdS QDs/TNTs, Au/TNTs, and TNTs. Furthermore, these results are in close contact with the results measured under ambient light (Figure 6a) and further assist the CV results by showing a negligible difference in the response current for all electrodes measured under the dark and ambient conditions. Figure S7b shows the calibration plots for the TNTs, Au/TNTs, CdS QDs/TNTs, and Au/CdS QDs/TNTs elecrodes derived from their corresponding amperometric response measured in the dark (Figure S7a). The sensitivity of the electrodes can be calculated from the slope of the linear fitting of the calibration curve, which is also mentioned in the plots. The Au/CdS/TNTs showed a sensitivity of 11,258 μA mM^{-1} cm^{-2}, which is slightly higher than that observed in ambient light (10,790 μA mM^{-1} cm^{-2}). These small variations in sensitivity can be neglected due to the fact that individual samples can show slight variations.

Electrochemical Detection of H_2O_2 on Au/CdS QDs/TNTs. The synergistic effects of Au/CdS QDs/TNTs for electrochemical analysis of H_2O_2 were evaluated by using CV. Figure 7a−d shows the CV for TNTs, Au/TNTs, CdS QDs/TNTs, and Au/CdS QDs/TNTs without and with the addition of different concentrations of H_2O_2. Pristine TNTs show (Figure 7a) a well-defined reduction peak at about −0.55 V by adding a small amount of H_2O_2 in PBS. An increase in the redox peak currents is also observed when increasing the H_2O_2 concentration within the electrolyte, which shows that the catalytic behavior of TNTs is favorable for the electrochemical detection of H_2O_2. The higher surface area of the nanochannels provided by the 1D nanotubes enhances the adsorption of the H_2O_2 molecules and accelerates the electrochemical reduction process for H_2O_2. The CV of Au/TNTs shows an enhanced peak intensity, while adding H_2O_2 in the electrolyte results in a further enhancement in the redox peak currents (Figure 7b). The Au NPs layer act as a co-catalyst that increases the conductivity of the biosensor and serves as an electron reservoir that rapidly initiates the degradation of the H_2O_2 and enhances the sensing response. Moreover, the Au NPs could stimulate the environment of the redox centers in cholesterol or H_2O_2 and promotes the electron transfer as a conduction center. The CdS QDs/TNTs (Figure 7c) further increase the redox peak current values for increasing H_2O_2 concentrations attributed to the smaller size of QDs and efficient charge transfer. The formation of junctions between CdS and TNTs acts as the directional electron transfer paths. The ternary heterostructure Au/CdS QDs/TNTs take the advantage of synergies of all the components of the electrode for a rapid and enhanced sensing activity as shown in Figure 7d. The above finding illustrates that the addition of different concentrations of H_2O_2 results in the increase of the reduction peak but at a different peak position (−0.55 V) as compared to cholesterol where the reduction peak was observed at about −1.2 V. This phenomenon can greatly improve the simultaneous detection of cholesterol and H_2O_2 and inhibits the interference caused by each other as well as by other biological molecules. On the other hand, a decrease in the oxidation peak was observed by increasing the concentration of H_2O_2, thereby indicating that the reduction of H_2O_2 is predominant.[5]

The effect of the potential scan rate on the oxidation and reduction peak currents in the presence of H_2O_2 was presented in Figure 7e. It can be seen that the oxidation and reduction currents increase by increasing the scan rate from 20 to 100 mV s^{-1}. The linear fitting of the redox peak current is presented in Figure 7f, which implies that the redox peak current is proportional to the root mean square of the scan rate indicating the diffusion-controlled process for H_2O_2 reduction at the electrode surface.

https://dx.doi.org/10.1021/acsami.0c19979
ACS Appl. Mater. Interfaces 2021, 13, 3653−3668

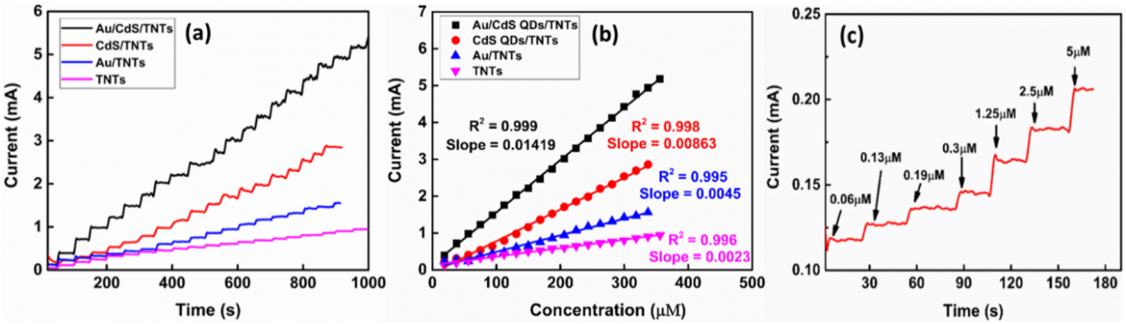

Figure 8. Amperometric response of the pristine TNTs, Au/TNTs, CdS QDs/TNTs, and Au/CdS QDs/TNTs at −0.55 V upon the successive addition of H_2O_2 in 40 mL of 0.1 M PBS at pH 7.0; (b) corresponding linear calibration curve electrodes w.r.t. H_2O_2 concentrations. (c) Amperometric response of the electrode toward a lower concentration of H_2O_2.

Table 2. Comparison of the Au/CdS QDs/TNTs H_2O_2 Biosensor with Other Electrode Systems

s. no.	electrode materials	LOD	sensitivity (μA mM^{-1} cm^{-2})	response time (s)	LDR	reference
1.	MoS_2 NPs/GC	2.5 nM	2580	5	5.0−100 nM	54
			160		100 nM−100 μM	
2.	MnO_2-VACNT	0.8 μM	1080		1.2 μM−1.8 mM	56
3.	MnO_2-OMC	0.07 μM	806.8		0.5 μM−0.6 mM	57
4.	3D GO-CO_3O_4PHs modified electrode	15 nM	3450	5	0.05−400 μM	5
			2120		450−1250 μM	
5.	RGO/ZnO GCE	0.02 μM	13,490	2	1−22.48 μM	58
6.	platinum hierarchical nanoflowers	0.32 μM	1390		10−400 μM	59
7.	GF/CO_3O_4-NPs/GCE	0.06 μM	1140	<10	0.2−211.5 μM	55
8.	α-Fe_2O_3-NPs-CH/GCE	0.4 μM	21,620		up to 44 μM	60
9.	NiO/MWCNTs	2 μM	1768.8	5	10 μM−7 mM	61
10.	Au/CdS QDs/TNTs	0.06 μM	78,833	5	18.73−355.87 μM	present work

The amperometric response of the pristine TNTs, Au/TNTs, CdS QDs/TNTs, and Au/CdS QDs/TNTs was tested for H_2O_2 by successively adding different volumes of the 15 mM stock solution in the electrolyte under an applied potential of −0.55 V (Figure 8a). A gradual small increase in the response current was obtained for the pristine TNTs in response to the addition of each concentration of H_2O_2. The hybrid system (Au/CdS QDs/TNTs), shows a much higher current response compared to the CdS QDs/TNTs and Au/TNTs electrode for different H_2O_2 concentrations. The hybrid electrodes possess a rapid decrease in the response time (from 8 to 5 s) in the order of TNTs > Au/TNTs > CdS QDs/TNTs > Au/CdS QDs/TNTs as shown in Table S2. Figure 8b shows the linear fitting of the calibration curves plotted for all the electrodes. The sensitivity of the Au/CdS QDs/TNTs (78,833 μA mM^{-1} cm^{-2}) electrode is 6-fold higher than that of the pristine TNTs. This is the highest sensitivity ever achived for the nonenzymatic electrochemical quantification of H_2O_2. Figure 8c shows the amperometric response of Au/CdS QDs/TNTs for the low concentrations of H_2O_2 where the electrode shows a significant current response for concentrations as low as 0.06 μM. The linear concentration range of 18.73−355.87 μM toward H_2O_2 detection for the Au/CdS QDs/TNTs electrode was obtained as shown in Figure 8c.

The electrochemical performance of the Au/CdS/TNTs electrode toward H_2O_2 detection was further compared with that of the H_2O_2 biosensors reported in the literature that are selected on the merits of higher sensitivity values. Sakthivel Kogularasu et al. have fabricated three-dimensional graphene oxide encapsulated cobalt oxide polyhedrons (3D GO-Co_3O_4 PHs) via the hydrothermal method for H_2O_2 detection, which exhibited a sensitivity of 3450 μA mM^{-1} cm^{-2}.[5] Tanyuan Wang and his co-workers have established MoS_2 nanoparticles deposited on a glassy carbon electrode for H_2O_2 detection (2580 μA mM^{-1} cm^{-2}).[54] Chelladurai Karuppiah and his co-workers have developed a graphene (GF) and cobalt oxide nanoparticles (Co_3O_4-NPs) composite modified electrode that exhibits a sensitivity of 1140 μA mM^{-1} cm^{-2} for H_2O_2 sensing.[55] Compared to all the reported data, the Au/CdS QDs/TNTs for the nonenzymatic detection of H_2O_2 exhibit a sensitivity of 78,833 μA mM^{-1} cm^{-2} with comparatively rapid response time and wide linear range of detection. Table 2 shows the comparison of the various parameters of the H_2O_2 sensors fabricated in this study with the ones reported in the literature.

The enhanced electrochemical activity of Au/CdS QDs/TNTs can be attributed to the following reasons. Decoration of TNTs with low band gap CdS QDs (2.4 eV) results in their suitable band gap alignment, which increases the efficiency of the charge transfer rate by reducing the electron traps within the electrode material. This idea was further complemented by a layer of Au NPs on the electrode surface that promotes electron transfer as a conduction center. The uniformly deposited CdS QDs and top layer of Au NPs on TNTs serve as the channels to facilitate the transfer of redox species at the electrode surface. The EIS data clearly indicate a decreasing trend in the diameter of the high-frequency semicircle due to the reduction in the charge transfer resistance for the hybrid Au/CdS QDs/TNTs system. Furthermore, the small size of CdS QDs provides a high surface area, thereby increasing the availability of active sites for the enhanced catalytic activities.

The CV and amperometry for TNTs, Au/TNTs, CdS QDs/TNTs, and Au/CdS QDs/TNTs were also evaluated under

https://dx.doi.org/10.1021/acsami.0c19979
ACS Appl. Mater. Interfaces 2021, 13, 3653−3668

Scheme 2. Schematic Illustration of the Oxidation Mechanism of Cholesterol and Reduction Mechanism of H_2O_2 on the Surface of Au/CdS QDs/TNTs

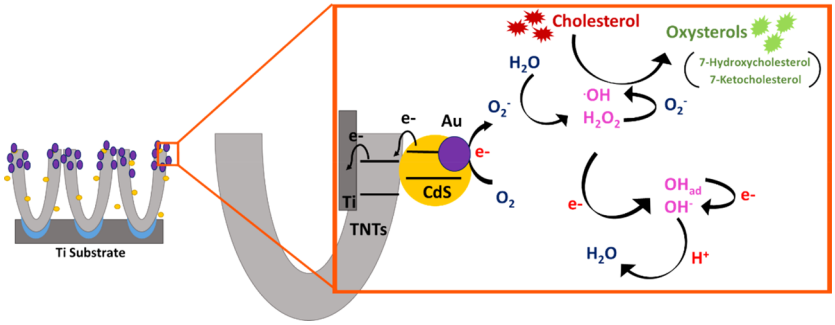

dark conditions for H_2O_2 detection. As depicted from the CV (Figure S8a–d), the results shows a very slight reduction in the redox peak current (with or without H_2O_2) under dark conditions when compared to ambient conditions (Figure 7a–d). Moreover, in CV, the redox peaks lie on the same potentials for all electrodes under ambient and dark conditions. However, compared to cholesterol, the difference in the CV curves for both conditions is a little bit more prominent, which can be attributed to the comparatively rapid and higher oxidation ability of H_2O_2 than cholesterol.

The amperometric response of TNTs, Au/TNTs, CdS QDs/TNTs, and Au/CdS QDs/TNTs for H_2O_2 detection in the dark is presented in Figure S9a, which shows a sequential increase in the response current by adding H_2O_2, and is in close proximity with the results measured in the ambient conditions. The corresponding calibration plots are presented in Figure S9b. These results show a slight decrease in the sensitivity for the dark (73,111 μA mM^{-1} cm^{-2}) as compared to ambient environment (78,833 μA mM^{-1} cm^{-2}). This fact can be attributed to the fact that H_2O_2 is a highly oxidizable material and can be reduced under ambient conditions, which thus also verifies the finding of CV in the dark.

Cholesterol can possibly be oxidized by two different approaches: (i) via abstraction of hydrogen from cholesterol by a free radical (•OH) or (ii) via cholesterol oxidation mediated by singlet oxygen.[62] The former mechanism can be employed by generating the free radicals inside the electrolyte by the heterogeneous transfer of electron between the surface of the electrode and the redox species. As CdS is an n-type semiconductor material where electrons are the majority charge carriers, under the applied negative potential, the energy of the electrons in the CB of CdS is raised and can be transferred to the oxygen molecules (O_2) at the surface of the electrode to yield O_2^- (eq 1). O_2^- further reacts with H_2O to produce H_2O_2 and hydroxyl radicals (•OH) (eqs 2 and 3).[63] These •OH radicals thus initiate the cholesterol auto-oxidation to produce oxysterols (7b-ketocholesterol, 7a-hydroxycholesterol, and 7b-hydroxycholesterol) (eq 4).[63,64] The H_2O_2 (produced during cholesterol oxidation or added as a second analyte within the electrolyte) at the surface of electrode can react with either the O_2^- or e^- to produce •OH radicals and OH^- (eqs 3 and 5). The complete mechanism for cholesterol oxidation and H_2O_2 reduction is illustrated in Scheme 2. In addition, it is to be noted that the amount of H_2O_2 produced during the cholesterol oxidation is not significant to show a prominent peak in the reverse scan of CV at low cholesterol concentrations (Figure 5d). When analyzing the CV of the Au/CdS QDs/TNTs electrode for cholesterol (Figure 5d) and H_2O_2 (Figure 7d) detection, it is observed that the redox peak for both analytes lies on completely different potentials. In other words, both cholesterol and H_2O_2 are electrochemically active on completely different onset potentials while using a single electrode system (Au/CdS QDs/TNTs). By switching the applied potential during amperometric studies between two different values, the sensing behavior of the biosensor could be specified for any one of the target analytes. In case of cholesterol detection, an applied potential of −1.2 V is utilized where the response current from H_2O_2 is critically minimized, which can be attributed to the relatively lower reduction potential of the H_2O_2 (−0.55 V). Moreover, the cholesterol is not oxidized at a potential of −0.55 V, which can greatly increase the selectivity of the biosensor.

$$CdS + O_2 + 2e^- \rightarrow 2CdS^+ + O_2^- \quad (1)$$

$$O_2^- + H_2O \rightarrow H_2O_2 + .\,OH \quad (2)$$

$$O_2^- + H_2O_2 \rightarrow .\,OH + OH^- + O_2 \quad (3)$$

$$OH + \text{cholesterol} \rightarrow \text{oxysterols} + e^- \quad (4)$$

The H_2O_2 was reduced in PBS on the surface of the electrode via the mechanism shown below.[43]

$$H_2O_2 + e^- \rightarrow OH_{ad} + OH^- \quad (5)$$

$$OH_{ad} + e^- \rightarrow OH^- \quad (6)$$

$$2OH^- + 2H^+ \rightarrow 2H_2O \quad (7)$$

Selectivity and Stability of the Au/CdS QDs/TNTs Biosensor. The capability of a biosensor to differentiate between the interfering species, with comparable electrochemical activities, and the target biomolecule is one of the most important factors that affect its performance. The two important factors that can influence the selectivity of the biosensor are the operational potential of the electrode and the concentration of the interferents. Figure 9a,b shows the amperometric response of the cholesterol and H_2O_2 detection in the presence of AA, urea, glucose, and L-cysteine in their physiological concentrations. In addition, the effect of the interference of the diluted samples of H_2O_2 on the response current for cholesterol detection (Figure 9a) was also studied. As the Au/CdS QDs/TNTs electrode operates on totally different potentials for both analytes, a sharp increase in the response current was obtained for cholesterol (at −1.2 V) with a significantly reduced interference signal from the diluted H_2O_2 [or vice versa (Figure 9b) at an applied potential of −0.55 V]. Moreover, the current response induced by the

https://dx.doi.org/10.1021/acsami.0c19979
ACS Appl. Mater. Interfaces 2021, 13, 3653−3668

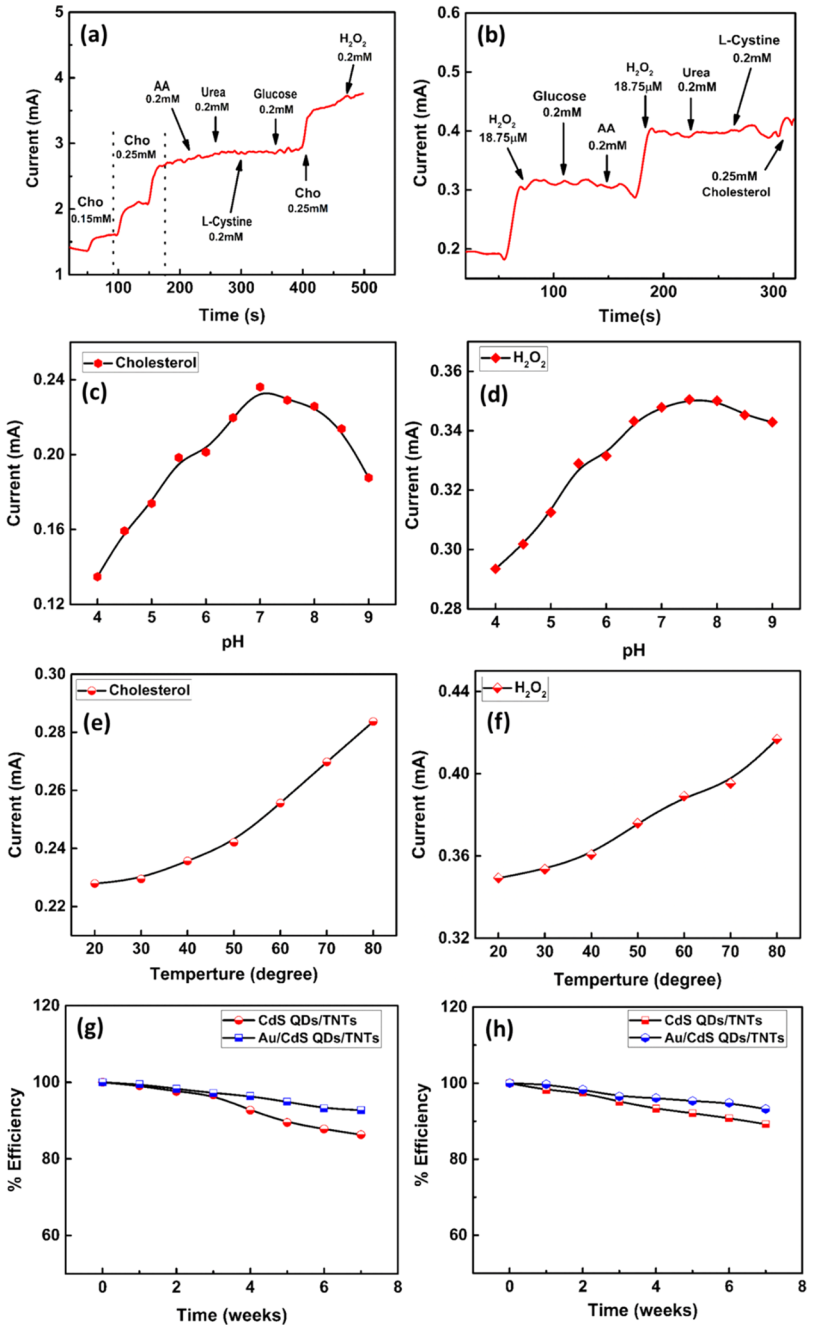

Figure 9. (a, b) Amperometric response of Au/CdS QDs/TNTs toward cholesterol and H_2O_2 with different interferents in 0.1 M PBS, respectively (pH 7.0). (c, d) Effect of pH, (e, f) temperature of the electrolyte on current response of the biosensor, and (g, h) shelf life (stability) curves of Au/CdS QDs/TNTs as a function of days for cholesterol and H_2O_2, respectively.

other interfering biomolecules is also negligible compared to the higher response of cholesterol (or H_2O_2), indicating the excellent selectivity of the proposed sensor for cholesterol (or H_2O_2) sensing. The possible reason for such a high selectivity can be the utilization of the negative potential where the aforementioned interfering species were not electrochemically active.[51,65−69]

The pH of the electrolyte has a strong influence on the performance of the electrochemical biosensor. The effect of the electrolyte pH value on the electrochemical behavior of the Au/CdS QDs/TNTs electrode was investigated for both analytes by CV in 0.1 M PBS as shown in Figure 9c,d. The oxidation peak current increases with pH, and the maximum peak current was obtained at pH 7.0 for cholesterol (Figure 9c) and at pH 7.5 for H_2O_2 (Figure 9d). A further increase in the pH value of the electrolyte results in the decreased oxidation current. Furthermore, the activity of the biosensor is reduced at low pH values; therefore, pH 7.0 was chosen as the optimized condition for further investigations.

The response current of the Au/CdS QDs/TNTs biosensor toward the varying temperatures in the range of 20−80 °C was investigated by CV in the presence of cholesterol and H_2O_2, respectively (Figure 9e,f). The oxidation current was found to be increased for both analytes by increasing the temperature due to the high reaction rate at the surface of the biosensor as a result of the fast diffusion process. These results demonstrated

https://dx.doi.org/10.1021/acsami.0c19979
ACS Appl. Mater. Interfaces 2021, 13, 3653−3668

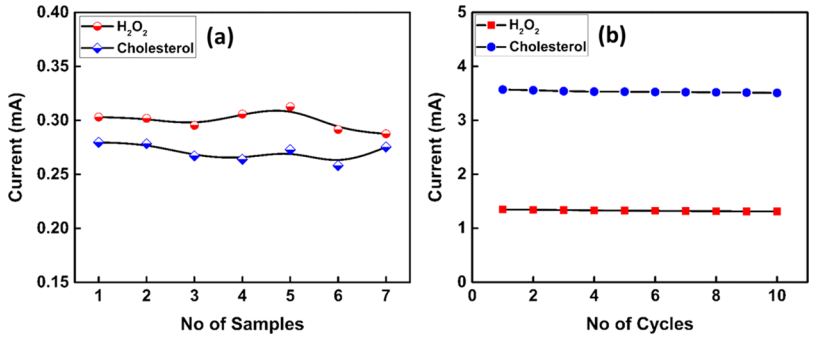

Figure 10. Calibration plot showing the (a) reproducibility and (b) repeatability of Au/CdS QDs/TNTs toward 240 μM cholesterol and 50 μM H_2O_2, respectively.

Table 3. Comparison of the Cholesterol and H_2O_2 Concentrations Detected in the Human Blood Serum Using the Reference and Proposed Methods

	cholesterol				H_2O_2			
sample	added (μM)	found (μM)	recovery	RSD (%)	added (μM)	found (μM)	recovery	RSD (%)
1	142.9	145.6	102.7	1.8	67.9	66.4	98.5	2.2
2	370.1	365.2	95.1	1.3	142.3	140.1	97.8	1.5
3	587.5	584.3	96.8	0.6	290.8	297.6	93.2	2.3

that the biosensor was highly stable over a temperature range with increasing catalytic activities.

Most of the metal oxide based biosensors suffer from a significant reduction in the electrochemical performance to the target biomolecules over a period of time. Therefore, the amperometric response of the Au/CdS QDs/TNTs biosensor was periodically checked by adding 150 μM cholesterol every seventh day over a period of 8 weeks (Figure 9g). The results indicate that the biosensor reported here retains 92.7% of its initial current even after 4 weeks, showing an about 6% increase in stability due to the Au NPs layer as compared to the CdS QDs/TNTs electrode. The stability of the biosensor toward the 18.75 μM H_2O_2 was also investigated as shown in Figure 9h. The results show that the fabricated biosensor holds about 93.2% of its initial response over the same time period compared to CdS QDs/TNTs (89.2%), thus suggesting a decent long-term stability of the biosensor for both analytes.

Repeatability and Reproducibility of the Au/CdS QDs/TNTs Biosensor. The reproducibility of the Au/CdS QDs/TNTs electrode for cholesterol and H_2O_2 detection was tested in seven individual samples prepared under similar experimental conditions (Figure 10a). An RSD value of about 2.7% for cholesterol and 1% for H_2O_2 was found from the data obtained from the amperometric response of both analytes. The consistency in the current response of the electrode toward the cholesterol and H_2O_2 was checked repeatedly using the biosensor for 10 times (Figure 10b). The electrode exhibited an acceptable RSD value of 1.5 and 3.6% for cholesterol and H_2O_2, respectively. This fact can be ascribed to the elimination of using enzymes in our system, which usually suffers from the short device lifetime due to the denaturing of enzymes. Moreover, this nonenzymatic biosensor can be used frequently for a number of times without deteriorating its catalytic activity and surface poisoning.

Real Sample Detection. The practicality and accuracy of the biosensor for clinical sample detection are of great importance. For this purpose, the proposed biosensor was employed for the quantification of cholesterol and H_2O_2 in human blood serum using the standard addition method. The serum was diluted in PBS (pH 7.0) prior to the assay to bring the concentration of cholesterol (and H_2O_2) under the linear calibration range. The serum samples were spiked with different concentrations of cholesterol and H_2O_2, and the recovery of the samples was measured. The values measured by the Au/CdS QDs/TNTs electrode for both analytes were in the acceptable range (Table 3), indicating that the proposed biosensor offers a great potential for practical application for the analysis of cholesterol and H_2O_2 in real clinical samples.

CONCLUSIONS

A sensitive, enzyme-free cholesterol and H_2O_2 sensor has been demonstrated using a biosensor composed of Au NPs deposited on CdS QDs decorated anodic TNTs. The incorporation of CdS QDs in TNTs not only provides a suitable band gap alignment for the fast electron transport but also, in combination with the Au NPs layer, serves as channels for the redox species from the redox center of both analytes toward the substrate. In addition, the TNTs functionalized with CdS QDs and Au NPs further increase the active surface area and offer an extremely sensitive detection of cholesterol (~10,790 μA mM^{-1} cm^{-2}) and H_2O_2 (78,833 μA mM^{-1} cm^{-2}) with a wide linear range (0.024−1.2 mM for cholesterol and 18.73−355.87 μM for H_2O_2) and fast response time. Moreover, the negative redox potential preserves the biosensor from interference of common interfering species, thus increasing the practicality of the biosensor for clinical sample analysis. In addition, the different redox potential for cholesterol and H_2O_2 detection may lead to a voltage-induced switchable biosensor for both analytes, thus increasing the practicality of the biosensor for clinical sample analysis. Our investigations demonstrate the potential use of Au/CdS QDs/TNTs in the nonenzymatic electrochemical detection of cholesterol and H_2O_2.

ASSOCIATED CONTENT

Supporting Information

The Supporting Information is available free of charge at https://pubs.acs.org/doi/10.1021/acsami.0c19979.

https://dx.doi.org/10.1021/acsami.0c19979
ACS Appl. Mater. Interfaces 2021, 13, 3653−3668

SEM images of the pristine TNTs after the second-step anodization and CdS(9) QDs/TNTs using the conventional SILAR method (Figure S1), SEM images of the top view of CdS QDs/TNTs for different deposition cycles (Figure S2), schematic illustration of the morphological evaluation of Au/CdS QDs/TNT in response to varying thicknesses of the sputtered Au layer and their thermal dewetting (Figure S3), SEM images of the top and cross-sectional view of Au/CdS QDs/TNTs for different film thicknesses of Au NPs layer (Figure S4), SEM images of the top and cross-sectional view of Au/TNTs (Figure S5), cyclic voltammetry of TNTs, Au/TNTs, CdS QDs/TNTs, and Au/CdS QDs/TNTs for electrochemical detection of cholesterol under dark and ambient conditions (Figure S6), comparison of various parameters presenting the performance of biosensor at different stages of fabrication for cholesterol sensing (Table S1), amperometric response and corresponding linear calibration curves of the different electrode configurations at −1.2 V upon successive addition of cholesterol under dark conditions (Figure S7), comparison of various parameters presenting the performance of the biosensor at different stages of fabrication for H_2O_2 sensing (Table 2), cyclic voltammetry of TNTs, Au/TNTs, CdS QDs/TNTs, and Au/CdS QDs/TNTs for electrochemical detection of H_2O_2 under dark and ambient conditions (Figure S8), amperometric response and corresponding calibration curves of the pristine TNTs, Au/TNTs, CdS QDs/TNTs, and Au/CdS QDs/TNTs at −0.55 V upon successive addition of H_2O_2 under dark conditions (Figure S9) (PDF)

AUTHOR INFORMATION

Corresponding Authors

Patrik Schmuki − *Department of Materials Science and Engineering, University of Erlangen-Nuremberg, D-91058 Erlangen, Germany; Department of Chemistry, King Abdulaziz University, Jeddah 21413, Saudi Arabia;* orcid.org/0000-0002-9208-5771; Email: schmuki@ww.uni-erlangen.de

Ghafar Ali − *Nanomaterials Research Group (NRG), Physics Division, PINSTECH, Islamabad 44000, Pakistan*; Email: ghafarali@kaist.ac.kr

Authors

Nilem Khaliq − *Department of Physics and Applied Mathematics, Pakistan Institute of Engineering and Applied Sciences (PIEAS), Islamabad 45650, Pakistan*

Muhammad Asim Rasheed − *Department of Physics and Applied Mathematics, Pakistan Institute of Engineering and Applied Sciences (PIEAS), Islamabad 45650, Pakistan*

Maaz Khan − *Nanomaterials Research Group (NRG), Physics Division, PINSTECH, Islamabad 44000, Pakistan*

Muhammad Maqbool − *Department of Clinical & Diagnostic Sciences, the University of Alabama at Birmingham, Birmingham, Alabama 35294, United States*

Mashkoor Ahmad − *Nanomaterials Research Group (NRG), Physics Division, PINSTECH, Islamabad 44000, Pakistan*

Shafqat Karim − *Nanomaterials Research Group (NRG), Physics Division, PINSTECH, Islamabad 44000, Pakistan*

Amjad Nisar − *Nanomaterials Research Group (NRG), Physics Division, PINSTECH, Islamabad 44000, Pakistan;* orcid.org/0000-0002-2196-1105

Sung Oh Cho − *Department of Nuclear and Quantum Engineering (NQe), KAIST, Daejeon 34141, South Korea;* orcid.org/0000-0002-5441-3244

Complete contact information is available at: https://pubs.acs.org/10.1021/acsami.0c19979

Notes

The authors declare no competing financial interest.

ACKNOWLEDGMENTS

The authors greatly acknowledge the Higher Education Commission (HEC) of Pakistan for providing financial support through an international research support initiative program (with grant no. I-8/HEC/HRD/2017/7726) for this research work. Financial support from DFG within the framework of its Excellence Initiative for the Cluster of Excellence "Engineering of Advanced Materials" under project no. 750302 is thankfully acknowledged.

REFERENCES

(1) Feng, D.; Li, L.; Han, X.; Fang, X.; Li, X.; Zhang, Y. Simultaneous Electrochemical Detection of Multiple Tumor Markers Using Functionalized Graphene Nanocomposites as Non-Enzymatic Labels. *Sens. Actuators, B* **2014**, *201*, 360−368.

(2) Ikonen, E. Mechanisms for Cellular Cholesterol Transport: Defects and Human Disease. *Physiol. Rev.* **2006**, *86*, 1237−1261.

(3) Maxfield, F. R.; Tabas, I. Role of Cholesterol and Lipid Organization in Disease. *Nature* **2005**, *438*, 612−621.

(4) Pratsinis, A.; Kelesidis, G. A.; Zuercher, S.; Krumeich, F.; Bolisetty, S.; Mezzenga, R.; Leroux, J.-C.; Sotiriou, G. A. Enzyme-Mimetic Antioxidant Luminescent Nanoparticles for Highly Sensitive Hydrogen Peroxide Biosensing. *ACS Nano* **2016**, *11*, 12210−12218.

(5) Kogularasu, S.; Govindasamy, M.; Chen, S. M.; Akilarasan, M.; Mani, V. 3D Graphene Oxide-Cobalt Oxide Polyhedrons for Highly Sensitive Non-Enzymatic Electrochemical Determination of Hydrogen Peroxide. *Sens. Actuators, B Chem.* **2017**, *253*, 773−783.

(6) Si, P.; Ding, S.; Yuan, J.; Lou, X. W.; Kim, D.-H. Hierarchically Structured One-Dimensional TiO2 for Protein Immobilization, Direct Electrochemistry, and Mediator-Free Glucose Sensing. *ACS Nano* **2011**, *5*, 7617−7626.

(7) Bao, S.-J.; Li, C. M.; Zang, J.-F.; Cui, X.-Q.; Qiao, Y.; Guo, J. New Nanostructured TiO 2 for Direct Electrochemistry and Glucose Sensor Applications. *Adv. Funct. Mater.* **2008**, *18*, 591−599.

(8) Fan, G. C.; Han, L.; Zhang, J. R.; Zhu, J. J. Enhanced Photoelectrochemical Strategy for Ultrasensitive DNA Detection Based on Two Different Sizes of CdTe Quantum Dots Cosensitized TiO2/CdS:Mn Hybrid Structure. *Anal. Chem.* **2014**, *86*, 10877−10884.

(9) Wu, H.; Fan, S.; Jin, X.; Zhang, H.; Chen, H.; Dai, Z.; Zou, X. Construction of a Zinc Porphyrin − Fullerene-Derivative Based Nonenzymatic Electrochemical Sensor for Sensitive Sensing of Hydrogen Peroxide and Nitrite. *Anal. Chem.* **2014**, *86*, 6285−6290.

(10) Yao, H.; Luo, X.; Yang, T.; Li, M.; Yang, B.; Lu, Y.; Liu, H. Triple-Switchable Biosensors and an AND Logic Gate Based on Binary Assembly of Weak Polyelectrolyte Multilayers and Hydrogel Films. *J. Electrochem. Soc.* **2016**, *163*, H1104−H1111.

(11) Raje, V. P.; Morgado, P. I.; Ribeiro, M. P.; Correia, I. J.; Bonifácio, V. D. B.; Branco, P. S.; Aguiar-Ricardo, A. Dual On-off and off-on Switchable Oligoaziridine Biosensor. *Biosens. Bioelectron.* **2013**, *39*, 64−69.

(12) Huang, J.; Zhang, L.; Liang, R. P.; Qiu, J. D. "On-off" Switchable Electrochemical Affinity Nanobiosensor Based on

Graphene Oxide for Ultrasensitive Glucose Sensing. *Biosens. Bioelectron.* **2013**, *41*, 430−435.
(13) Chang, H. C.; Ho, J. A. A. Gold Nanocluster-Assisted Fluorescent Detection for Hydrogen Peroxide and Cholesterol Based on the Inner Filter Effect of Gold Nanoparticles. *Anal. Chem.* **2015**, *87*, 10362−10367.
(14) Wei, Y.; Zeng, Q.; Huang, J.; Hu, Q.; Guo, X.; Wang, L. An Electro-Responsive Imprinted Biosensor with Switchable Affinity toward Proteins. *Chem. Commun.* **2018**, *54*, 9163−9166.
(15) Zhang, R.; Chen, X.; Sun, Z.; Chen, S.; Gao, J.; Sun, Y.; Li, H. Switchable Nanochannel Biosensor for H2S Detection Based on an Azide Reduction Reaction Controlled BSA Aggregation. *Anal. Chem.* **2019**, *91*, 6149−6154.
(16) Sharma, V.; Mobin, S. M. Cytocompatible Peroxidase Mimic CuO:Graphene Nanosphere Composite as Colorimetric Dual Sensor for Hydrogen Peroxide and Cholesterol with Its Logic Gate Implementation. *Sens. Actuators, B Chem.* **2017**, *240*, 338−348.
(17) Dey, R. S.; Raj, C. R. Development of an Amperometric Cholesterol Biosensor Based on Graphene-Pt Nanoparticle Hybrid Material. *J. Phys. Chem. C* **2010**, *114*, 21427−21433.
(18) Lin, X.; Ni, Y.; Kokot, S. Electrochemical Cholesterol Sensor Based on Cholesterol Oxidase and MoS 2 -AuNPs Modified Glassy Carbon Electrode. *Sens. Actuators, B* **2016**, *233*, 100−106.
(19) Gao, Z.; Han, Y.; Wang, Y.; Xu, J.; Song, Y. Nanoporous NiO / TiO 2 Layers and Its Use in Non-Enzymatic Glucose Sensing. *Nature* **2013**, *3*, 3323−3329.
(20) Ali, M. A.; Srivastava, S.; Solanki, P. R.; Reddy, V.; Agrawal, V. V.; Kim, C.; John, R.; Malhotra, B. D. Highly Efficient Bienzyme Functionalized Nanocomposite-Based Microfluidics Biosensor Platform for Biomedical Application. *Sci. Rep.* **2013**, *3*, 1−9.
(21) Cheng, W. L.; Sue, J. W.; Chen, W. C.; Chang, J. L.; Zen, J. M. Activated Nickel Platform for Electrochemical Sensing of Phosphate. *Anal. Chem.* **2010**, *82*, 1157−1161.
(22) Li, Z.; Zhang, Y.; Ye, J.; Guo, M.; Chen, J.; Chen, W. Nonenzymatic Glucose Biosensors Based on Silver Nanoparticles Deposited on TiO_2 Nanotubes. *J. Nanotechnol.* **2016**, *2*, 1−7.
(23) Tian, J.; Li, Y.; Dong, J.; Huang, M.; Lu, J. Photoelectrochemical TiO2 Nanotube Arrays Biosensor for Asulam Determination Based on In-Situ Generation of Quantum Dots. *Biosens. Bioelectron.* **2018**, *110*, 1−7.
(24) Hu, L.; Fong, C. C.; Zhang, X.; Chan, L. L.; Lam, P. K. S.; Chu, P. K.; Wong, K. Y.; Yang, M. Au Nanoparticles Decorated TiO2Nanotube Arrays as a Recyclable Sensor for Photoenhanced Electrochemical Detection of Bisphenol A. *Environ. Sci. Technol.* **2016**, *50*, 4430−4438.
(25) Mun, K. S.; Alvarez, S. D.; Choi, W. Y.; Sailor, M. J. A Stable, Label-Free Optical Interferometric Biosensor Based on TiO2 Nanotube Arrays. *ACS Nano* **2010**, *4*, 2070−2076.
(26) Lu, J.; Li, H.; Cui, D.; Zhang, Y.; Liu, S. Enhanced Enzymatic Reactivity for Electrochemically Driven Drug Metabolism by Confining Cytochrome P450 Enzyme in TiO_2 Nanotube Arrays. *Anal. Chem.* **2014**, *86*, 8003−8009.
(27) Guo, C.; Huo, H.; Han, X.; Xu, C.; Li, H. Ni/CdS Bifunctional Ti@TiO_2Core−Shell Nanowire Electrode for High-Performance Nonenzymatic Glucose Sensing. *Anal. Chem.* **2013**, *86*, 876−883.
(28) Dhyani, H.; Azahar Ali, M.; Pandey, M. K.; Malhotra, B. D.; Sen, P. Electrophoretically Deposited CdS Quantum Dots Based Electrode for Biosensor Application. *J. Mater. Chem.* **2012**, *22*, 4970−4976.
(29) Guo, C.; Huo, H.; Han, X.; Xu, C.; Li, H. Ni/CdS Bifunctional Ti@TiO2 Core-Shell Nanowire Electrode for High-Performance Nonenzymatic Glucose Sensing. *Anal. Chem.* **2013**, *86*, 876−883.
(30) Wang, X. F.; Zhou, Y.; Xu, J. J.; Chen, H. Y. Signal-on Electrochemiluminescence Biosensors Based on CdS-Carbon Nanotube Nanocomposite for the Sensitive Detection of Choline and Acetylcholine. *Adv. Funct. Mater.* **2009**, *19*, 1444−1450.
(31) Yue, Z.; Lisdat, F.; Parak, W. J.; Hickey, S. G.; Tu, L.; Sabir, N.; Dorfs, D.; Bigall, N. C. Quantum-Dot-Based Photoelectrochemical Sensors for Chemical and Biological Detection. *ACS Appl. Mater. Interfaces* **2013**, *5*, 2800−2814.
(32) Zeng, X.; Tu, W.; Li, J.; Bao, J.; Dai, Z. Photoelectrochemical Biosensor Using Enzyme-Catalyzed in Situ Propagation of CdS Quantum Dots on Graphene Oxide. *ACS Appl. Mater. Interfaces* **2014**, *6*, 16197−16203.
(33) Zhao, W. W.; Chen, R.; Dai, P. P.; Li, X. L.; Xu, J. J.; Chen, H. Y. A General Strategy for Photoelectrochemical Immunoassay Using an Enzyme Label Combined with a CdS Quantum Dot/ TiO2Nanoparticle Composite Electrode. *Anal. Chem.* **2014**, *86*, 11513−11516.
(34) Zhang, L.; Sun, Y.; Liang, Y. Y.; He, J. P.; Zhao, W. W.; Xu, J. J.; Chen, H. Y. Ag Nanoclusters Could Efficiently Quench the Photoresponse of CdS Quantum Dots for Novel Energy Transfer-Based Photoelectrochemical Bioanalysis. *Biosens. Bioelectron.* **2016**, *85*, 930−934.
(35) Tang, L.; Zhu, Y.; Yang, X.; Sun, J.; Li, C. Self-Assembled CNTs/CdS/Dehydrogenase Hybrid-Based Amperometric Biosensor Triggered by Photovoltaic Effect. *Biosens. Bioelectron.* **2008**, *24*, 319−323.
(36) Pan, Z. Q.; Fan, H.; Shi, C. G.; Bao, N.; Yu, C. M.; Gu, H. Y. Direct Electrochemistry of Hemoglobin Immobilized on CdS:Mn Nanoparticles. *Microchim. Acta* **2011**, *173*, 277−283.
(37) Huang, Y.; Zhang, W.; Xiao, H.; Li, G. An Electrochemical Investigation of Glucose Oxidase at a CdS Nanoparticles Modified Electrode. *Biosens. Bioelectron.* **2005**, *21*, 817−821.
(38) Dhyani, H.; Dhand, C.; Malhotra, B. D. Polyaniline-CdS Quantum Dots Composite for Mediator Free Biosensing. *J. Biosens. Bioelectron.* **2012**, *03*, 1−9.
(39) Yu, J.; Gong, C.; Wu, Z.; Wu, Y.; Xiao, W.; Su, Y.; Sun, L.; Lin, C. Efficient Visible Light-Induced Photoelectrocatalytic Hydrogen Production Using CdS Sensitized TiO_2Nanorods on TiO_2Nanotube Arrays. *J. Mater. Chem. A* **2015**, *3*, 22218−22226.
(40) Dong, K.; He, J.; Liu, J.; Li, F.; Yu, L.; Zhang, Y.; Zhou, X.; Ma, H. Photocatalytic Performance of Cu2O-Loaded TiO2/RGO Nanoheterojunctions Obtained by UV Reduction. *J. Mater. Sci.* **2017**, *52*, 6754−6766.
(41) Li, W.; Li, M.; Xie, S.; Zhai, T.; Yu, M.; Liang, C.; Ouyang, X.; Lu, X.; Li, H.; Tong, Y. Improving the Photoelectrochemical and Photocatalytic Performance of CdO Nanorods with CdS Decoration. *CrystEngComm* **2013**, *15*, 4212.
(42) Hou, J.; Yang, C.; Wang, Z.; Jiao, S.; Zhu, H. Hydrothermal Synthesis of CdS/CdLa2S4 heterostructures for Efficient Visible-Light-Driven Photocatalytic Hydrogen Production. *RSC Adv.* **2012**, *2*, 10330.
(43) Gowthaman, N. S. K.; Sinduja, B.; John, S. A. Tuning the Composition of Gold-Silver Bimetallic Nanoparticles for the Electrochemical Reduction of Hydrogen Peroxide and Nitrobenzene. *RSC Adv.* **2016**, *6*, 63433−63444.
(44) Huang, Q.; Loveridge, M. J.; Genieser, R.; Lain, M. J.; Bhagat, R. Electrochemical Evaluation and Phase-Related Impedance Studies on Silicon-Few Layer Graphene (FLG) Composite Electrode Systems. *Sci. Rep.* **2018**, *8*, 1386.
(45) Cho, E. J.; Bright, F. V. Optical Sensor Array and Integrated Light Source. *Anal. Chem.* **2001**, *73*, 3289−3293.
(46) Zhang, J.; Li, B.; Zhang, L.; Jiang, H. An Optical Sensor for Cu(Ii) Detection with Upconverting Luminescent Nanoparticles as an Excitation Source. *Chem. Commun.* **2012**, *48*, 4860−4862.
(47) Li, Y.; Bai, H.; Liu, Q.; Bao, J.; Han, M.; Dai, Z. A Nonenzymatic Cholesterol Sensor Constructed by Using Porous Tubular Silver Nanoparticles. *Biosens. Bioelectron.* **2010**, *171-172*, 2356−2379.
(48) Lee, Y.-J.; Park, J.-Y. Nonenzymatic Free-Cholesterol Detection via a Modified Highly Sensitive Macroporous Gold Electrode with Platinum Nanoparticles. *Biosens. Bioelectron.* **2010**, *26*, 1353−1358.
(49) Yang, J.; Lee, H.; Cho, M.; Nam, J.; Lee, Y. Nonenzymatic Cholesterol Sensor Based on Spontaneous Deposition of Platinum Nanoparticles on Layer-by-Layer Assembled CNT Thin Film. *Sens. Actuators, B* **2012**, *171−172*, 374−379.

https://dx.doi.org/10.1021/acsami.0c19979
ACS Appl. Mater. Interfaces 2021, 13, 3653−3668

(50) Matsui, T.; Kitagawa, Y.; Okumura, M.; Shigeta, Y. Accurate Standard Hydrogen Electrode Potential and Applications to the Redox Potentials of Vitamin C and NAD / NADH. *J. Phys. Chem. A* **2015**, *119*, 369−376.
(51) Singh, R. K.; Schechter, A. Electrochemical Investigation of Urea Oxidation Reaction on β Ni(OH)2 and Ni/Ni(OH)2. *Electrochim. Acta* **2018**, *278*, 405−411.
(52) Ji, R.; Wang, L.; Wang, G.; Zhang, X. Synthesize Thickness Copper (I) Sulfide Nanoplates on Copper Rod and It's Application as Nonenzymatic Cholesterol Sensor. *Electrochim. Acta* **2014**, *130*, 239−244.
(53) Saha, M.; Das, S. Fabrication of a Nonenzymatic Cholesterol Biosensor Using Carbon Nanotubes from Coconut Oil. *J. Nanostruct. Chem.* **2014**, *4*, 94.
(54) Wang, T.; Zhu, H.; Zhuo, J.; Zhu, Z.; Papakonstantinou, P.; Lubarsky, G.; Lin, J.; Li, M. Biosensor Based on Ultrasmall MoS_2Nanoparticles for Electrochemical Detection of H_2O_2Released by Cells at the Nanomolar Level. *Anal. Chem.* **2013**, *85*, 10289−10295.
(55) Karuppiah, C.; Palanisamy, S.; Chen, S.-M.; Veeramani, V.; Periakaruppan, P. A Novel Enzymatic Glucose Biosensor and Sensitive Non-Enzymatic Hydrogen Peroxide Sensor Based on Graphene and Cobalt Oxide Nanoparticles Composite Modified Glassy Carbon Electrode. *Sens. Actuators, B Chem.* **2014**, *196*, 450−456.
(56) Xu, B.; Ye, M. L.; Yu, Y. X.; Zhang, W. D. A Highly Sensitive Hydrogen Peroxide Amperometric Sensor Based on MnO_2-Modified Vertically Aligned Multiwalled Carbon Nanotubes. *Anal. Chim. Acta* **2010**, *674*, 20−26.
(57) Luo, L.; Li, F.; Zhu, L.; Zhang, Z.; Ding, Y.; Deng, D. Non-Enzymatic Hydrogen Peroxide Sensor Based on MnO_2-Ordered Mesoporous Carbon Composite Modified Electrode. *Electrochim. Acta* **2012**, *77*, 179−183.
(58) Palanisamy, S.; Chen, S.-M.; Sarawathi, R. A Novel Non-enzymatic Hydrogen Peroxide Sensor Based on Reduced Graphene Oxide / ZnO Composite Modified Electrode. *Sens. Actuators, B Chem* **2012**, *166-167*, 372−377.
(59) Heli, H.; Sattarahmady, N.; Vais, R. D.; Mehdizadeh, A. R. Enhanced Electrocatalytic Reduction and Highly Sensitive Non-enzymatic Detection of Hydrogen Peroxide Using Platinum Hierarchical Nanoflowers. *Sens. Actuators, B* **2014**, *192*, 310−316.
(60) Zhang, L.; Ni, Y.; Wang, X.; Zhao, G. Direct Electrocatalytic Oxidation of Nitric Oxide and Reduction of Hydrogen Peroxide Based on α-Fe2O3 Nanoparticles-Chitosan Composite. *Talanta* **2010**, *82*, 196−201.
(61) Zhang, W.-D.; Chen, J.; Jiang, L.-C.; Yu, Y.-X.; Zhang, J.-Q. A Highly Sensitive Nonenzymatic Glucose Sensor Based on NiO-Modified Multi-Walled Carbon Nanotubes. *Microchim. Acta* **2010**, *168*, 259−265.
(62) Prochazka, M.; Stupavska, M.; Jerigova, M.; Velic, D. TiO2Photocatalytic Degradation of Cholesterol: SIMS Study. *Surf. Interface Anal.* **2013**, *45*, 22−26.
(63) Lee, J. H.; Shoeman, D. W.; Kim, S. S.; Csallany, A. S. The Effect of Superoxide Anion in the Production of Seven Major Cholesterol Oxidation Products in Aptoric and Protic Conditions. *Int. J. Food Sci. Nutr.* **2009**, *48*, 151−159.
(64) Morzycki, J. W.; Sobkowiak, A. Electrochemical Oxidation of Cholesterol. *Beilstein J. Org. Chem.* **2015**, *11*, 392−402.
(65) Yang, Q.; Long, M.; Tan, L.; Zhang, Y.; Ouyang, J.; Liu, P.; Tang, A. Helical TiO2Nanotube Arrays Modified by Cu−Cu2O with Ultrahigh Sensitivity for the Nonenzymatic Electro-Oxidation of Glucose. *ACS Appl. Mater. Interfaces* **2015**, *7*, 12719−12730.
(66) Liu, M.; Liu, R.; Chen, W. Graphene Wrapped Cu2O Nanocubes : Non-Enzymatic Electrochemical Sensors for the Detection of Glucose and Hydrogen Peroxide with Enhanced Stability. *Biosens. Bioelectron.* **2013**, *45*, 206−212.
(67) Boggs, B. K.; King, R. L.; Botte, G. G. Urea Electrolysis: Direct Hydrogen Production from Urine. *Chem. Commun.* **2009**, *2009*, 4859−4861.
(68) Hallaj, R.; Salimi, A.; Akhtari, K.; Soltanian, S.; Mamkhezri, H. Electrodeposition of Guanine Oxidation Product onto Zinc Oxide Nanoparticles : Application to Nanomolar Detection of l -Cysteine. *Sensors Actuators B* **2009**, *135*, 632−641.
(69) Bao, S. J.; Li, C. M.; Zang, J. F.; Cui, X. Q.; Qiao, Y.; Guo, J. New Nanostructured TiO2 for Direct Electrochemistry and Glucose Sensor Applications. *Adv. Funct. Mater.* **2008**, *18*, 591−599.

https://dx.doi.org/10.1021/acsami.0c19979
ACS Appl. Mater. Interfaces 2021, 13, 3653−3668